
1 **A 1-km daily surface soil moisture dataset of enhanced coverage**
2 **under all-weather conditions over China in 2003-2019**

3 Peilin Song^{1,4†}, Yongqiang Zhang^{1*}, Jianping Guo^{2*}, Jiancheng Shi³, Tianjie
4 Zhao⁴, Bing Tong²

5 ¹ Key Laboratory of Water Cycle and Related Land Surface Processes, Institute of Geographic Sciences
6 and Natural Resources Research, The Chinese Academy of Sciences, Beijing 100101, China

7 ² State Key Laboratory of Severe Weather, Chinese Academy of Meteorological Sciences, Beijing
8 100081, China

9 ³ National Space Science Center, Chinese Academy of Sciences, Beijing 100190, China

10 ⁴ State Key Laboratory of Remote Sensing Science, Aerospace Information Research Institute, Chinese
11 Academy of Sciences. Beijing 100101, China

12 [†] now at School of Electronic Science and Engineering, Xi'an Jiaotong University, Xi'an, 710049, China

13

14 *Correspondence to: Yongqiang Zhang (zhangyq@igsnrr.ac.cn); Jianping Guo (jpguo@cma.gov.cn)

15

16

17

18

19

20

21

22 **Abstract:**

23 Surface soil moisture (SSM) is crucial for understanding the hydrological process of
24 our earth surface. Passive microwave (PM) technique has long been the primary tool
25 for estimating global SSM from the view of satellite, while the coarse resolution
26 (usually $>\sim 10$ km) of PM observations hampers its applications at finer scales.
27 Although quantitative studies have been proposed for downscaling satellite PM-based
28 SSM, very few products have been available to public that meet the qualification of 1-
29 km resolution and daily revisit cycles under all-weather conditions. In this study, we
30 developed one such SSM product in China with all these characteristics. The product
31 was generated through downscaling the AMSR-E/AMSR-2 based SSM at 36-km,
32 covering all on-orbit time of the two radiometers during 2003-2019. MODIS optical
33 reflectance data and daily thermal infrared land surface temperature (LST) that had
34 been gap-filled for cloudy conditions were the primary data inputs of the downscaling
35 model, so that the “all-weather” quality was achieved for the 1-km SSM. Daily images
36 from this developed SSM product have quasi-complete coverage over the country
37 during April-September. For other months, the national coverage percentage of the
38 developed product is also greatly improved against the original daily PM observations,
39 through a specifically developed sub-model for filling the gap between seams of
40 neighboring PM swaths during the downscaling procedure. The product is well
41 compared against *in situ* soil moisture measurements from 2000+ meteorological
42 stations, indicated by station averages of the unbiased RMSD ranging from 0.052

43 vol/vol to 0.059 vol/vol. Moreover, the evaluation results also show that the developed
44 product outperforms the SMAP-Sentinel (Active-Passive microwave) combined SSM
45 product at 1-km, with a correlation coefficient of 0.55 achieved against that of 0.40 for
46 the latter product. This indicates the new product has great potential to be used for
47 hydrological community, agricultural industry, water resource and environment
48 management.

49 **1. Introduction**

50 Surface soil moisture (SSM) is one of the most important variables that dominate
51 the mass and energy cycles of earth surface system (Entekhabi et al., 2010b). Satellite-
52 based SSM datasets of sufficiently fine spatio-temporal resolutions over large-scale
53 areas have significant implication on improved investigations at various research fields
54 including hydrological signature identification (Zhou et al., 2021; Jung et al., 2010),
55 agricultural yield production estimation (Ines et al., 2013; Pan et al., 2019),
56 drought/waterlogging monitoring and warning (Vergopolan et al., 2021; Den Besten et
57 al., 2021; Jing and Zhang, 2010), as well as weather prediction and future climate
58 analysis (Koster et al., 2010; Jeffrey et al., 2001). Microwave bands with centimeter-
59 level or longer wavelengths (X-band, C-band, and L-band) are currently identified as
60 the primary band channels suitable for SSM observations from view of satellite, due to
61 their high penetration capabilities through cloud layers and vegetation canopies. In
62 terms of sensor types, microwave SSM detection includes passive microwave
63 (radiometer-based) techniques and active microwave (radar, scatterometer) techniques.

64 Satellite-based passive microwave (PM) radiometers, e.g. the Soil Moisture Active
65 Passive (SMAP), the Soil Moisture and Ocean Salinity (SMOS), and the Advance
66 Microwave Scanning Radiometer-2 (AMSR-2), can obtain SSM observations at a
67 revisit interval of 1-3 days, with relatively poor native spatial resolutions of tens of
68 kilometers. Active microwave (AM) such as radar can achieve kilometer-level and even
69 finer resolution of observations targeting at the earth surface. However, this usually
70 sacrifices the swath width of radar configuration, because of which, most satellite-based
71 synthetic aperture radars (SAR) have an obviously longer global revisit cycle (usually
72 longer than 5 days, e.g. Sentinel-1 SAR data) than the typical radiometers. Moreover,
73 AM radar backscatter signals are extremely sensitive to speckle noise (Entekhabi et al.,
74 2016), as well as influence from soil roughness, vegetation canopy structure and water
75 content (Piles et al., 2009). All above influential factors have seriously impeded the use
76 of AM radar techniques or combination of passive/active microwave datasets for
77 producing high spatial resolution SSM products with a frequent revisit.

78 Apart from microwave signals, solar reflectance or ground emission signals
79 originated from optical and infrared band domains also have the potential to reflect
80 SSM variation. Based on optical/infrared bands, however, SSM is typically estimated
81 based on indirect relationships through intermediate variables like soil evaporation
82 (Komatsu, 2003), vegetation condition (Zeng et al., 2004), or soil thermal inertia
83 (Verstraeten et al., 2006). To overcome the spatio-temporally instable performance on
84 SSM modelling that might be brought by such indirect relationships, they are typically
85 fused with the PM SSM datasets. In this manner, it can well reconcile the advantage of

86 PM observations with respect to its high sensitivity to SSM variation, as well as that of
87 optical/infrared observations with respect to its finer spatial resolutions at kilometer- or
88 even hectometer-levels. Such data fusion techniques are also known as downscaling
89 techniques of PM remote sensing SSM. Archetypal downscaling models include the
90 “universal triangle feature space (UTFS)”-based models (Chauhan et al., 2003; Choi
91 and Hur, 2012; Sanchez-Ruiz et al., 2014), the “DISaggregation based on a Physical
92 And Theoretical scale CHange (DISPACTH)” model (Merlin et al., 2010; Merlin et al.,
93 2005; Merlin et al., 2013; Merlin et al., 2008), and the “University of California, Los
94 Angeles (UCLA)” model (Peng et al., 2016). The physics of these models are mainly
95 based on the response of SSM variation to changes in soil evaporation or land surface
96 evapotranspiration. Another significant branch of such downscaling models are based
97 on the sensitivity of SSM to soil thermal inertia, which is quantified by diurnal LST
98 difference estimated from thermal-infrared wave bands (Fang and Lakshmi, 2013; Fang
99 et al., 2018).

100 Sabaghy et al. (2020) have shown that using optical and infrared data can achieve
101 finer-resolution SSM estimates which are better consistent with ground soil moisture
102 records, compared with using the radar datasets. Moreover, considering the short revisit
103 cycle (daily) of optical/infrared sensors onboard typical polar-orbit satellites, using
104 optical/infrared datasets to downscale PM SSM should be among the optimal methods
105 for obtaining SSM data with high spatio-temporal resolutions over national, continental,
106 or global scales. On the other hand, satellite remote sensing SSM products that are
107 characterized by 1-km resolution of daily revisit intervals and stable long time series

108 dating back to at least 15-20 years ago, are urgently required for accelerating the
109 development of various research fields, especially agriculture industry, water resources
110 management, and hydrological disaster monitoring (Sabaghy et al., 2020; Mendoza et
111 al., 2016). However, very seldom sets of such data products are publicly available to
112 the remote sensing research community because of the following drawbacks. First,
113 there is a serious lack of cloud-free optical/infrared imagery, which means the method
114 cannot deliver any SSM downscaling under cloudy/rainy weather. Second, most of the
115 above-mentioned optical/infrared-data-based downscaling methods were mainly
116 evaluated at regional or even smaller scales. This might raise concern on the
117 universality of those methods. For example, the DISPATCH method has been
118 recognized to be less effective in humid (energy-limited) regions compared with in arid
119 and semi-arid (water-limited) regions (Molero et al., 2016; Song et al., 2021; Zheng et
120 al., 2021). As far as the UTFS-based method is concerned, a poorer performance was
121 obtained compared to the DISPATCH in a typical water-limited region in North
122 America, according to the experiment conducted by Kim and Hogue (2012).

123 To improve the above-mentioned issues, we produced an all-weather daily SSM
124 data product at 1-km resolution all over China during 2003-2019, based on fusion of
125 multiple remote sensing techniques, including reconstruction of optical/infrared
126 observations under cloud as well as an improved PM SSM downscaling methodology
127 proposed in our previous study (Song et al., 2021). The potential significance of this
128 study includes

129 (i) to better serve and investigate the land surface hydrology processes and their
130 sophisticated interactions to human society at multi-scale (from national to regional)
131 resolutions in China because the country covers about 1/15 of the global terrestrial area
132 with about 1/5 of the world population, and
133 (ii) to provide a methodology framework that can inspire future studies on
134 generating similar SSM datasets all over the globe, based on the plentifulness of
135 resources on climate type, land covers, and topography in China.

136

137 **2. Methods and Materials**

138 **2.1 Datasets**

139 **2.1.1 PM SSM data**

140 Spatial downscaling of PM SSM is the fundamental theory for constructing the
141 target finer-resolution data product in this study. Therefore, the native retrieval
142 accuracy of the coarse-resolution PM SSM data product, based on which the
143 downscaling procedures are performed, is considerably crucial to the performance of
144 the downscaled data product (Busch et al., 2012; Im et al., 2016; Kim and Hogue, 2012).

145 Although the L-band PM brightness temperature (TB) observed by satellite missions
146 such as SMAP or SMOS are considered more suitable for SSM retrieval compared with
147 C- or X-band TB, both above missions started their space operations in the 2010s. This
148 means that to obtain downscaled SSM of longer historical periods, we still require to
149 rely on other C-/X-band-based radiometers which started their operations earlier than

150 SMAP and SMOS. An optimal satellite PM TB observation system dating back to
151 earlier years of this century is composed of the “Advanced Microwave Scanning
152 Radiometer of the Earth Observing System (AMSR-E)”, together with its successor of
153 AMSR-2. AMSR-E operated during 2002-2011 onboard the Aqua satellite which is
154 governed by National Aeronautics and Space Administration (NASA), whilst AMSR-
155 2 is operating onboard the Global Change Observation Mission1-Water (GCOM-W1)
156 satellite developed by the Japan Aerospace Exploration Agency (JAXA) since 2012.

157 Several classical PM SSM retrieval algorithms have been applied to the afore-
158 mentioned “AMSR series (including AMSR-E and AMSR-2)” TB for generating long-
159 term global SSM products at 25 km (Table 1), including the JAXA algorithm (Fujii et
160 al., 2009; Koike et al., 2004), the “Land Parameter Retrieval Model (LPRM)” algorithm
161 (Song et al., 2019b; Meesters et al., 2005; Owe et al., 2001), and the algorithm
162 developed by the University of Montana (UMT) (Jones et al., 2009; Du et al., 2016). A
163 recent AMSR-based night-time SSM product during 2002-2019 has been produced
164 through a neural network trained against SMAP radiometer-based descending SSM
165 (hereafter referred to as “NN-SM product”) (Yao et al., 2021). The global validation
166 results show that this NN-SM product is better than the JAXA and LPRM products.

167 Besides, the NN-SM has also been compared with another long-term ~25-km all-
168 weather SSM dataset generated through the European Space Agency (ESA)’s Climate
169 Change Initiative (CCI) program. The ESA-CCI SSM product is different from the rest
170 products mentioned above in that it was implemented by fusion of observations from
171 comprehensive AM- and PM-based satellite sensors, rather than only relying on the

172 radiometers of AMSR series. According to Yao et al. (2021), the ESA-CCI SSM has
173 slightly better validation accuracy than the NN-SM product, but the number of available
174 observations per pixel cell in an entire year is much smaller for the ESA-CCI SSM in
175 Southeast China. In view of all above coarse-resolution SSM data products, we finally
176 selected the NN-SM product to implement the following spatial downscaling
177 procedures rather than the ESA-CCI SSM, to make a balance between data accuracy
178 and data availability per year. We have also made additional evaluations within China
179 in Section Appendix-A to ensure the relatively outstanding performance of the NN-SM
180 product as described above.

181 Table 1 Information of all-weather microwave remote sensing coarse-resolution SSM data

182 products that can be potentially downscaled to obtain fine resolution SSM.

Name	Resolution	Satellite radiometers involved	Data availability (URL)
NN-SM	36 km (by the product	AMSR-E/ AMSR-2 EASE Grid (2002-2011, 2012-present) projection)	https://data.tpdc.ac.cn/en/data/c26201fc-526c-465d-bae7-5f02fa49d738/
ESA-CCI v6.1	0.25°	AMSR-E/ AMSR-2/ SMOS/ WindSat/ SMMR/ SSM/I/ TMI (1978-2020)	https://www.esa-soilmoisture-cci.org/v06.1_release
JAXA product	0.25° / 0.1°	AMSR-E/ AMSR-2 (2002-2011, 2012-present)	https://gportal.jaxa.jp/
LPRM	0.25° / 0.1°	AMSR-E/ AMSR-2 (2002-2011, 2012-present)	https://search.earthdata.nasa.gov/
UMT product	25 km (by the EASE Grid (2002-present) projection)	AMSR-E/ AMSR-2	http://files.ntsg.umt.edu/data/LPDR_v2/

184 2.1.2 Optical remote sensing data and digital elevation model (DEM)

185 Optical remote sensing datasets provide finer spatial texture information on the
186 daily basis for the downscaling purpose of PM SSM. Such data that can be used as
187 inputs of our SSM product processing line are mainly provided by the Moderate-
188 resolution Imaging Spectroradiometer (MODIS) onboard the Terra and Aqua satellites.

189 Specifically, they involve the 1-km daily night-time Aqua MODIS LST product
190 (MYD21A1N.v061) and the 500-m daily “Bidirectional Reflectance Distribution
191 Function (BRDF)” - Adjusted Reflectance dataset (MCD43A4.v061). MYD21A1 LST

192 data can be recognized as a crucial proxy of land surface thermal capacity (Fang et al.,
193 2013) and soil evaporative rate (Merlin et al., 2008). The MCD43A4 nadir reflectance
194 product, with view angle effect corrected using the BRDF model, is capable to provide

195 observations from visible to shortwave-infrared bands that can characterize water
196 content variation of the bare soils as well as the vegetation canopy. Overall, the above-
197 mentioned datasets were selected primarily because they deliver indicators (land

198 surface thermal capacity, soil evaporative rate, or vegetation condition) that can well
199 response to soil moisture dynamics from different aspects. Prior to being employed for

200 SSM downscaling, conventional pre-processing procedure of pixel quality check was
201 applied for both optical products by screening out pixels not classed as “good quality”,
202 according to the 8-bit “Quality Assessment (QA)” field of each spectral band. Moreover,
203 to normalize their natively different spatial resolutions, all MCD43A4 based reflectance

204 values at the 500-m pixel level were upscaled to the sinusoidally projected MODIS 1-
205 km grids using their spatial averages.

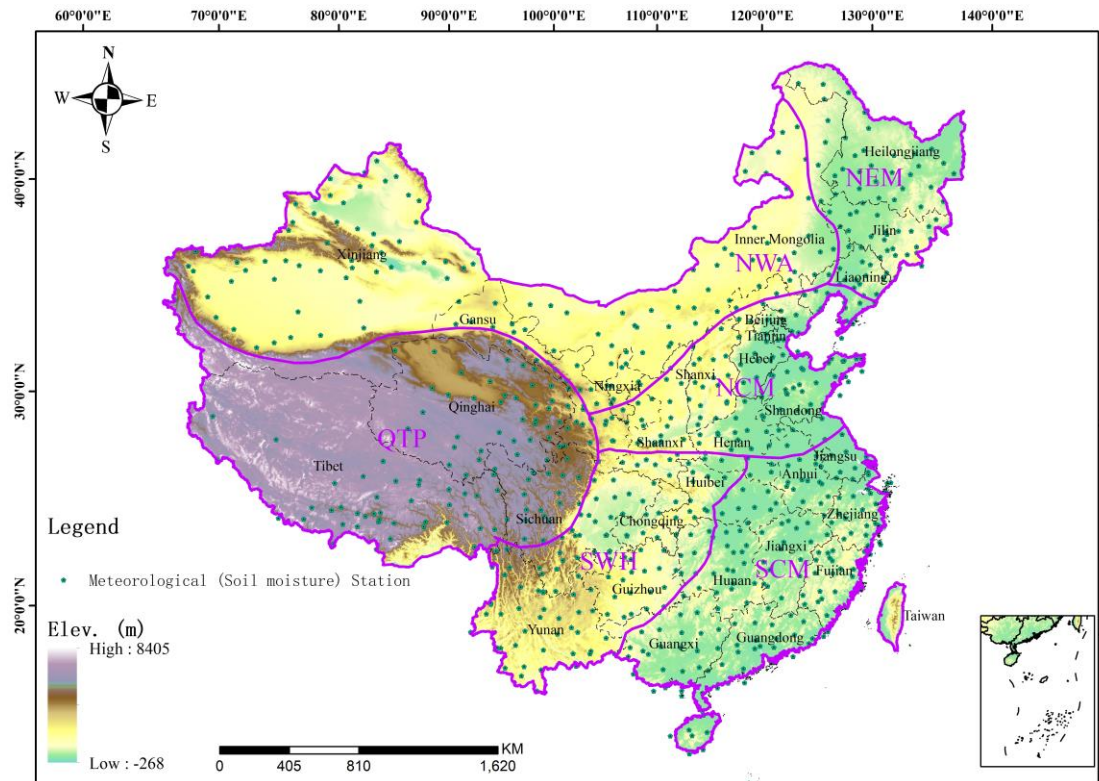
206 Apart from MODIS optical remote sensing data, all 90-m DEM tiles generated by
207 the NASA Shuttle Radar Topography Mission (SRTM; <http://srtm.csi.cgiar.org/>, last
208 access: July 10, 2020) were mosaicked all over China and then employed as another
209 essential input variable for the procedures as described by Section 2.2.2 below. Similar
210 to that applied to the MCD43A4 product, spatial upscaling in correspondence to the
211 MODIS 1-km grids is also an indispensable pre-processing step for the mosaicked
212 DEM data.

213 2.1.3 Study area and validation data

214 Our study area is set up as the total terrestrial extent of China. To comprehensively
215 evaluate the SSM downscaling performances for different geographic regions (see
216 Section 3.3), we divided the country further into six different geographic-climate
217 regions using elevation, precipitation, hydrogeology, vegetation type, and topography.
218 The six regions include the Northeast Monsoon (NEM) region, the Northwest Arid
219 (NWA) region, the Qinghai–Tibet Plateau (QTP) region, the North China Monsoon
220 (NCM) region, the South China Monsoon (SCM) region, and the Southwest Humid
221 (SWH) region. The detailed delimitation principle of these geographic-climate regions
222 was originally described in Meng et al. (2021). The geographic zoning map is shown
223 in Fig. 1, while the corresponding shapefile boundary files can be accessed from the

224 Resource and Environment Science and Data Center of the Chinese Academy of
225 Sciences (<http://www.resdc.cn/>, last access: May 22, 2021).

226



227

228 Fig. 1 The geographic zoning map of China (delineated using the purple color) superposed with
229 topographic information, as well as general locations for the 756 basic meteorological stations
230 (<http://data.cma.cn/>, last access: January 20, 2021) that provide partial benchmark measurements for
231 SSM and LST validation in this study.

232 We utilized ground soil moisture measurements for validating the downscaled
233 remote sensing SSM product at the local scale. The ground measurements are derived
234 from 2417 meteorological stations (including 756 basic stations of the National Climate
235 Observatory and 1661 regionally intensified stations) of over China, as partially shown
236 in Fig. 1. The soil moisture measurement devices in these stations, with uniform
237 observation standards, are instrumented under the national project of “Operation

238 Monitoring System of Automatic Soil Moisture Observation Network in China (Wu et
239 al., 2014)”, the construction of which has been led by China Meteorological
240 Administration since 2005. Until 2016, all stations have been in operation for
241 automatically observing hourly in situ soil moisture dynamics at eight different depth
242 ranges (0-10 cm, 10-20 cm, 20-30 cm, 30-40 cm, 40-50 cm, 50-60 cm, 70-80 cm, 90-
243 100 cm). It has also been widely used by previous studies for evaluating satellite soil
244 moisture estimates in China (Meng et al., 2021; Chen et al., 2020; Zhang et al., 2014;
245 Zhu and Shi, 2014). In our current study, ground measurements matching the shallowest
246 depth range (0-10 cm) from the initial time of each station until the end of 2019 are
247 employed as validation benchmark of the satellite SSM retrievals. At the temporal
248 dimension, measurements made at 1:00 A.M. and 2:00 A.M are averaged, in order to
249 match the mean satellite transit time of 1:30 A.M. for AMSR descending observations.

250 Moreover, 0-cm top ground temperatures are simultaneously measured at all these
251 meteorological stations on the daily basis, at the local time windows of 2:00 A.M./P.M.
252 and 10:00 A.M./P.M., respectively. We therefore exploited such measurements
253 recorded at 2:00 A.M. to validate the cloud gap-filled night-time (~1:30 A.M.) LST
254 estimates over the Aqua-MODIS based 1-km pixels containing these stations (see
255 Section 2.2.2). Our primary validation period covers the entire years of 2017, 2018, and
256 2019.

257 In addition to the ground soil moisture measurements, the SMAP Level3
258 radiometer-based daily 36-km SSM product
259 (<https://dx.doi.org/10.5067/OMHVSRGFX38O>) in its descending orbit scenes (at

260 ~6:00 A.M. of local time) from 2016 to 2019, was employed as another complementary
261 validation benchmark. This dataset is potential for providing more comprehensive
262 evaluations to our developed product at regional/national scales, especially on account
263 of its notably creditable performance (see Fig. A1 in Appendix A). The latest version
264 of this dataset (SPL3SMP, Version 8) contains soil moisture retrievals based on
265 different algorithms including the dual channel algorithm and the single channel
266 algorithm. In this study we only extracted SSM estimates derived with the dual channel
267 algorithm because this algorithm was reported to outperform the single channel
268 algorithm over some agricultural cropland core validation sites (O'neill et al., 2021).

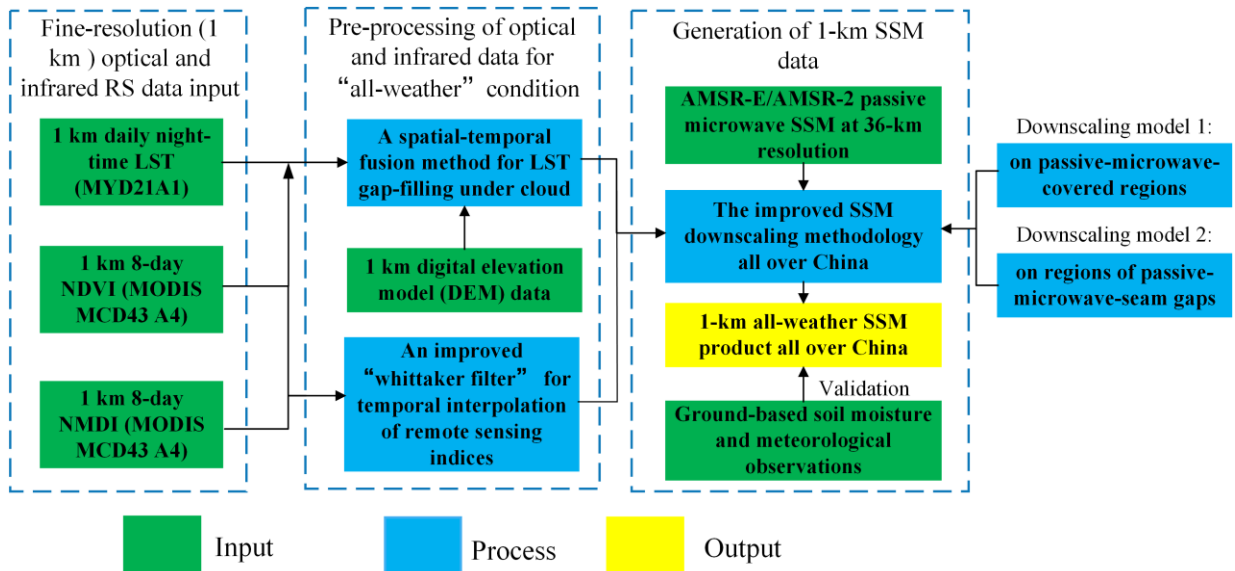
269 2.1.4 Ancillary SSM products for comparison

270 In order to comprehensively demonstrate the validation performance of our
271 proposed SSM product, there is necessity to make an inter-comparison against similar
272 existing datasets. In this regard, we introduced the Level2 SMAP/Sentinel Active-
273 Passive combined SSM product on 1-km earth-fixed grids, i.e., the SPL2SMAP_S_V3
274 dataset (Das et al., 2020), and used its validation performance against in-situ
275 measurements throughout the years of 2017, 2018, and 2019, as a baseline to better
276 evaluate our proposed SSM product. The SPL2SMAP_S_V3 dataset contains global
277 SSM at resolutions of 3 km and 1 km respectively, which were disaggregated from the
278 SMAP radiometer-based SSM retrievals of 36-km/9-km footprints in conjunction with
279 the high-resolution Sentinel-1 C-band radar backscatter coefficients (Das et al., 2019).
280 To our knowledge, this dataset is possibly the only publicly available product which

281 can provide global remote sensing SSM estimates at the 1-km resolution. The sentinel
282 backscatter coefficient inputs for this product are only those received in the descending
283 orbit scenes (at ~6:00 A.M. of local time), whilst the closest SMAP SSM retrievals
284 from either ascending (at ~6:00 P.M. of local time) or descending orbits are used to
285 spatially match up with the sentinel-1 scene. It is noticed that at the descending
286 observation time the soil moisture vertical profile has approached a hydrostatic balance
287 (Montaldo et al., 2001), thereby providing the optimal chance for soil moisture fusion
288 and validation with observations at different soil depths. Therefore, we only selected
289 the 1-km disaggregated SSM estimates based on descending SMAP SSM retrievals (i.e.,
290 the subset with field name of ‘disagg_soil_moisture_1 km’ in the SPL2SMAP_S_V3
291 dataset). Meanwhile, the 0-10 cm in-situ soil moisture measurements observed at 6:00
292 A.M. and the SMAP radiometer-based descending SSM estimates were employed as
293 the validation benchmarks, in a manner similar to that applied to our proposed SSM
294 product (Section 2.1.3).

295 **2.2 Methodology**

296 The general methodological framework for producing the all-weather daily 1-km
297 SSM product is shown as in Fig. 2, with details described in the following context of
298 this section.



299
300

Fig. 2 The overall methodological framework of this study.

301 2.2.1 Reconstruction of thermal-infrared LST and remote sensing (vegetation)

302 indices under cloud

303 Reconstruction of missing pixels under cloud in the optical remote sensing input
 304 datasets is the prerequisite for achieving the “all-weather” property of the final
 305 downscaled SSM output. For reconstructing thermal-infrared LST, we adopted the
 306 cloud gap-filling method as proposed by our previous study (Song et al., 2019a). This
 307 method, also referred to as a typical “spatio-temporal data fusion” (STDF) method
 308 (Dowling et al., 2021), was built using clear-sky LST observations of spatially
 309 neighboring pixels observed at proximal dates, with concurrent NDVI and DEM also
 310 employed as additional data inputs. The STDF method can be expressed as follows:

$$311 \quad LST_{t_1}^* = a \times LST_{t_0}^* + b \times NDVI_{t_1}^* + c \times DEM^* + d \quad (1)$$

312 Where the superscript “*” indicates that this variable has been normalized to the range
 313 0 to 1.0 (Song et al., 2019a), based on the maximum and minimum values of that
 314 variable found across China (excluding invalid values representing states of snow, ice,
 315 and water bodies). Parameters a , b , c , and d are coefficients fitted between all pixels
 316 with clear-sky LST estimates on a specific date t_1 ($LST_{t_1}^*$) and their counterparts on

317 one proximal date, t_0 ($LST^*_{t_0}$). $NDVI^*_{t_1}$ indicates the corresponding (normalized) NDVI
318 on the t_1 date calculated using the MCD43A4 daily product. After deriving the
319 coefficients of a , b , c , and d , Equation (1) was used to fill all cloudy MODIS LST pixels
320 on the t_1 date. For any t_1 date included in the study period, the t_0 date was iterated among
321 all neighboring dates of t_1 meeting the condition $|t_0 - t_1| \leq 30$ (from the nearest date to
322 the furthest date). The average of estimated LST values for t_0 was then taken where a
323 cloud gap pixel was filled more than once (based on the iterative t_0 dates). The iteration
324 was stopped when the fraction of pixels with effective LST values on t_1 was equal to or
325 exceeded 0.99.

326 An important flaw of this STDF method should be noticed with regard to
327 potentially existential bias of the cloud gap-filled LST outputs, because the outputs
328 represent theoretically reconstructed LST under clear sky rather than under the real
329 cloudy condition. Another of our previous studies (Dowling et al., 2021) concerning
330 this STDF method proposed a follow-up step, which incorporated PM-derived surface
331 temperature, to adjust that bias. In our current production pipeline, however, this
332 follow-up step for cloud bias adjustment in LST was not carried out. This is because
333 the results in Section Appendix-B show that using LST generated by the STDF alone
334 leads to more accurate SSM outcomes in general. The possible reasons for this are
335 discussed in Section 4.2.

336 Reconstruction of the remote sensing vegetation indices under cloudy conditions,
337 including NDVI and MNDI, was simply based on the modified time series filter of the
338 Whittaker Smoother (MWS) as developed by Kong et al. (2019). This is reasonable
339 because the dynamic trends of vegetation growth are relatively less volatile compared
340 to LST on the daily basis, and can thus be gap-filled for missing values using a time-
341 series-filtering-like algorithm.

342 2.2.2 Improved downscaling technique of SSM based on fusion of PM and
343 optical/infrared data

344 The core component of the SSM downscaling methodology is an improved linking
345 model between PM SSM and (fine-resolution) optical remote sensing observations.
346 This model enhances the relatively poorer performance of the conventional DISPATCH
347 in energy-limited regions, whilst maintains the generally good quality of the
348 DISPATCH in water-limited ones. Therefore, the improved model is more appropriate
349 to be applied in China which contains a wide range of geographical settings, compared
350 to other conventional downscaling models. Since this model origins from our previous
351 study (Song et al., 2021), herein we simply give its mathematical expression as follows:

352

$$SSM = \frac{a \times \ln(1 - SEE)}{1 - b \times NMDI} + c \quad (2)$$

353 In Equation (2), *SEE* denotes “soil evaporative efficiency” and is a mathematical
354 function of LST and the typical Normalized Difference Vegetation Index (NDVI), with
355 its specific form described in Merlin et al. (2008). NMDI is another remote sensing
356 index calculated as $\frac{R_{infr,860nm} - (R_{sw,1600nm} - R_{sw,2100nm})}{R_{infr,860nm} + (R_{sw,1600nm} - R_{sw,2100nm})}$ (Wang and Qu, 2007).
357 $R_{infr,860nm}$, $R_{infr,1600nm}$, and $R_{infr,2100nm}$ represent land surface reflectance signals
358 derived from three different MODIS-MCD43A4 based near-infrared/shortwave-
359 infrared bands, with their wavelengths centering at 860 nm, 1600 nm, and 2100 nm
360 respectively. The parameters *a*, *b*, and *c* are empirical coefficients that represent
361 background information of local soil texture and vegetation types. In Song et al. (2021),
362 these coefficients have been fitted and calibrated based on multi-temporal observations
363 at the PM pixel scale. In our current study, however, we have discovered that coupling

364 of multiphase observations at both the spatial and the temporal dimensions can lead to
365 more optimal solution of the coefficients, as they can produce downscaled SSM images
366 with notably declined effect of ‘mosaic’ against the original PM 36-km pixels.

367 Therefore, the modified optimal cost function χ^2 for deriving these coefficients is re-
368 defined as follows:

$$369 \chi^2 = \sum_{d=-dl}^{dl} \sum_{i=0}^{N=ws \times ws} w_i \times (SSM_{ob,i,d} - SSM_{mod,i,d})^2 \quad (3)$$

370 Through the cost function, the spatial extent of each 36-km pixel P_0 on any arbitrary
371 date D_0 obtains a unique set of coefficients. As shown by Equation (3), all pixels were
372 exploited within the spatial square window (with its side length equal to ws) centered
373 at P_0 ranging from $-dl$ -th day to dl -th day relative to the date of D_0 . To determine the
374 optimum values for dl and ws , we have tested each member in the collection of [3, 5, 7,
375 9, 11, 13] for both parameters. Evaluation against in-situ data indicates that the
376 optimum dl and ws are 5 and 7, respectively (results are similar to what is shown in
377 Section 3.2, but not presented here). SSM_{ob} and SSM_{mod} denote the AMSR NN-SM 36-
378 km SSM observations as well as SSM observations modelled by Equation (2) based on
379 upscaled optical datasets, respectively. w_i is a weight coefficient used to ensure that
380 neighboring observations near the centering pixel P_0 play more dominating roles as
381 compared with the far-end pixels in the cost function, considering the “Tobler’s First
382 Law of Geography (Sui, 2004)”. w_i is calculated using an adaptive bi-square function:

$$383 w_i = \begin{cases} \left[1 - \left(\frac{dis_i}{b}\right)^2\right]^2, & dis_i < b \\ 0, & dis_i \geq b \end{cases} \quad (4)$$

384 where dis_i indicates the distance between the i -th pixel and the centering pixel P_0 . b is
385 named as the adaptive kernel bandwidth of the bi-square function (Duan and Li, 2016),
386 and is optimized as 200 km through using a cross validation method as recommended
387 by Brunsdon et al. (1996).

388 With the linking model obtained, we can subsequently utilize the spatial
389 downscaling relationship function to produce 1-km fine resolution SSM. The
390 downscaling relationship function is constructed by transforming the linking model into
391 its Taylor expansion formula and preserving all components with respect to the input
392 optical variables of the linking model at first and second orders. This relationship is
393 inspired from Malb  teau et al. (2016) and Merlin et al. (2010), and is mathematically
394 described below:

$$395 SSM_{1\text{-}km} = SSM_{36\text{km}} + \left(\frac{\partial SSM}{\partial SEE} \right)_{36\text{km}} \times (SSE_{1\text{km}} - \langle SSE \rangle_{36\text{km}}) + 0.5 \times \left(\frac{\partial^2 SSM}{\partial SEE^2} \right) \times (SSE_{1\text{km}} - \langle SSE \rangle_{36\text{km}})^2 + \left(\frac{\partial SSM}{\partial NMDI} \right)_{36\text{km}} \times (NMDI_{1\text{km}} - \langle NMDI \rangle_{36\text{km}}) + 0.5 \times \left(\frac{\partial^2 SSM}{\partial NMDI^2} \right) \times (NMDI_{1\text{km}} - \langle NMDI \rangle_{36\text{km}})^2 \quad (5)$$

398 In the above relationship, $\langle \rangle$ denotes the spatial averaging operator for all of the 1-km
399 optical remote sensing input variables within the corresponding 36-km pixel,
400 $\frac{\partial SSM}{\partial SEE} \left(\frac{\partial^2 SSM}{\partial SEE^2} \right)$ and $\frac{\partial SSM}{\partial NMDI} \left(\frac{\partial^2 SSM}{\partial NMDI^2} \right)$ respectively denoting the first-(second-) order
401 partial derivative of the linking model described in Equation (2).

402 It should be noticed that there exist middle-/low-latitude gap regions between
403 seams of neighboring daily AMSR-E(-2) swaths, indicating that $SSM_{36\text{km}}$ in Equation
404 (5) is not always available on the daily basis (Song and Zhang, 2021a). For such PM-
405 seam gaps on a particular date t_0 , the corresponding $SSM_{36\text{km},t_0}$ in Equation (5) is

406 substituted by $0.5 \times (SSM_{36km,t0+1} + SSM_{36km,t0-1}) + \Delta SSM_{36km,t0}$. Herein $SSM_{36km,t0-1}$
407 and $SSM_{36km,t0+1}$ respectively denote the SSM estimate before and after the date of t_0 .
408 $\Delta SSM_{36km,t0}$ is a component for correcting inter-day bias, with the following expression:

409
$$\Delta SSM_{36km,t0} = SSM(SEE_{36km,t0}, NMDI_{36km,t0}) -$$
 (6)
$$0.5 \times (SSM(SEE_{36km,t0-1}, NMDI_{36km,t0-1}) + SSM(SEE_{36km,t0+1}, NMDI_{36km,t0+1}))$$

410 In the above equation, $SSM(SEE_{36km}, NMDI_{36km})$ denotes SSM that is directly
411 modelled based on Equation (1) using 36-km SEE and NMDI. The 36-km SEE and
412 NMDI are obtained via averaging the variables spatially from their native resolution at
413 1-km. If all SSM_{36km} during the three consecutive days (t_0-1 , t_0 , and t_0+1) are missing
414 due to other extreme conditions like snow, ice, or surface dominated by substantially
415 large water bodies, the downscaling process cannot be fulfilled and all 1-km sub-pixels
416 with the SSM_{36km} have to be set as null values.

417 2.2.3 Evaluation metrics

418 We employed the classic metrics of ‘Root Mean Square Difference (RMSD)’ and
419 correlation coefficient (r -value) for evaluating satellite-based (SSM and LST) estimates
420 against ground measurements. Herein RMSD is not referred to as ‘Root Mean Square
421 Error (RMSE)’, although the latter term shares the same definition and has been used
422 more commonly in previous studies. This is because both ground observations and
423 other benchmark data (i.e. SMAP radiometer-based SSM) may also present
424 measurement uncertainties in practice. For SSM evaluation, the unbiased RMSD, or
425 ubRMSD (Entekhabi et al., 2010a; Molero et al., 2016), is calculated instead of RMSD
426 when validated against ground soil moisture measurements. This can better investigate

427 the time series similarity between satellite and in situ datasets by eliminating the
428 systematic bias caused by spatial scale mismatch between them.

429 The above-mentioned classic metrics are primarily suitable to evaluate the
430 absolute reliability of an independent remote sensing product. However, we also require
431 another metric for characterizing the relative improvement of the downscaled SSM
432 estimates against the original PM observations on capturing local soil moisture
433 dynamics. For this purpose, we employed the “gain metric” of G_{down} , which was
434 developed particularly by Merlin et al. (2015) for assessment of soil moisture
435 downscaling methodology. G_{down} is a comprehensive indicator for evaluating gains of
436 the downscaled SSM against the original coarse-resolution PM data in terms of their
437 mean bias, bias in variance (slope), and time series correlation with ground benchmark.
438 It has a valid domain between -1 and 1, with positive (negative) value indicating
439 improved (deteriorated) spatial representativeness of the downscaled SSM against the
440 original PM data. Detailed definition and introduction of G_{down} are given in Equation
441 (8) and Section 3.3 of Merlin et al. (2015).

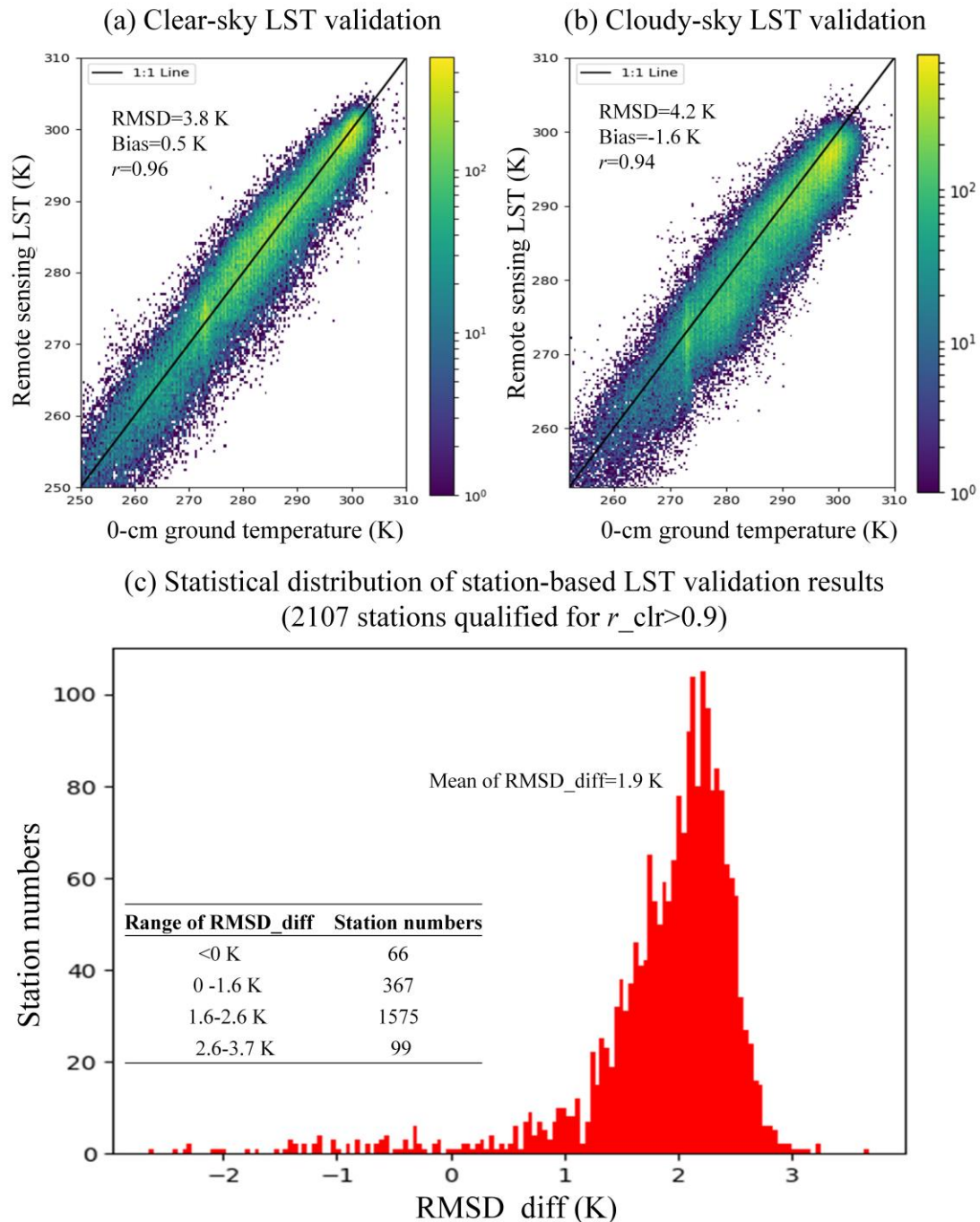
442 **3. Results**

443 **3.1 Evaluation on reconstructed thermal-infrared LST under**
444 **cloud**

445 The meteorological-station-based validation of reconstructed 1-km thermal-
446 infrared LST under cloud were preliminarily fulfilled, to ensure the high quality of input
447 dataset variables for SSM downscaling. Since disadvantageous effects might be

448 brought to this validation campaign by the potentially existing heterogeneity of the
449 validated 1-km thermal-infrared remote sensing pixels, we firstly analyzed correlations
450 between estimated and benchmark datasets at each station, only based on satellite
451 remote sensing observations obtained under clear sky. Stations that have their
452 correlation coefficients (r_{clr}) lower than 0.9 herein have to be screened out because there
453 exist higher chances of cross-scale spatial mismatch within and around these stations
454 in terms of the land surface thermal properties. Among all 2417 stations (see Section
455 2.1.3) where 0-cm in-situ top-ground temperature measurements were available, we
456 finally preserved 2107 stations characterized by $r_{clr} > 0.9$. In the subsequent step, remote
457 sensing LST under cloud and under clear-sky conditions were respectively validated at
458 these stations, with the results revealed in Fig. 3. It is manifested through Fig. 3-(a) and
459 -(b) that very close performances have been achieved between the clear-sky and the
460 cloudy scenarios, especially considering their almost equally high validating
461 correlations between 0.94-0.96. For each independent station, we calculated the
462 “RMSD difference (RMSD_diff)” between the two scenarios, based on the formula of
463 “ $RMSD_{clr} - RMSD_{cld}$ (the subscripts of ‘clr’ and ‘cld’ denote clear-sky and cloudy
464 conditions separately)”. The statistical distribution of this RMSD difference with regard
465 to different stations is shown in Fig. 3-(c). Apparently, 1942 stations all over the country
466 have obtained an RMSD difference value below 2.6 K, and the mean RMSD difference
467 is about 1.9 K. All above results have indicated that the uncertainty of our night-time
468 LST reconstruction algorithm proposed for cloudy conditions is not very significant.

469 The corresposive uncertainty that could be propagated to downscaled SSM in this
 470 stage is analyzed below in Section 3.2.



471

472 Fig. 3 validation results of the cloud gap-filled LST in China. (a) Density plot of thermal infrared
 473 LST under clear-sky condition compared to the 0-cm ground temperature measurements for all
 474 stations. (b) Same to (a) but for thermal infrared LST under cloudy conditions. (c) Statistical

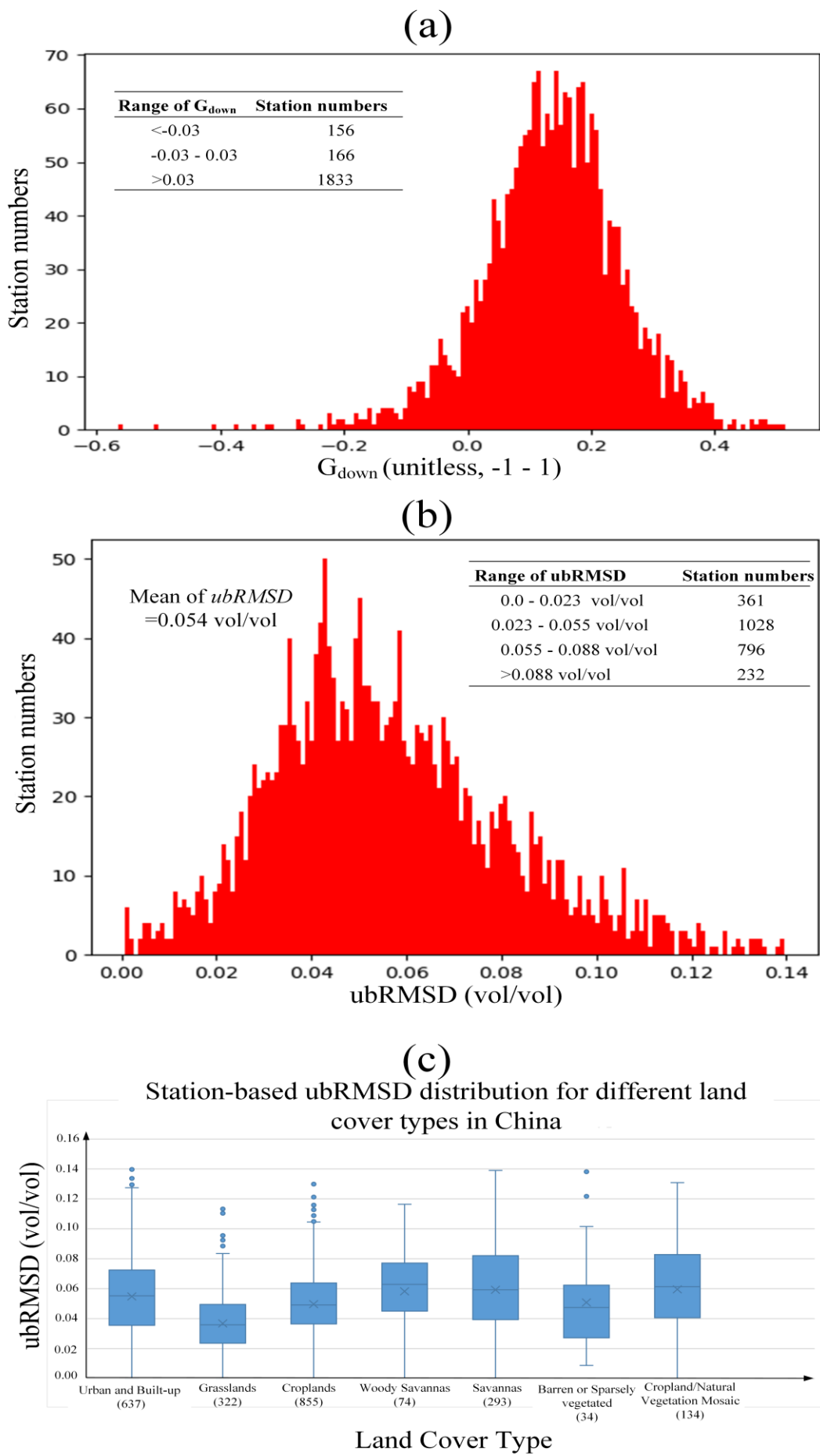
475 distribution of difference between RMSD of clear-sky LST and RMSD of gap-filled LST under cloudy
476 condition with regard to different meteorological stations over the study region.

477

478 3.2 Evaluation on the final 1-km SSM product

479 The overall validation results of the finally downscaled 1-km SSM product against
480 ground soil moisture data is demonstrated in Fig. 4. Fig. 4-(a) shows that about 85%
481 (N: 1833) of the total 2154 stations (the remaining 263 stations are located in pixels
482 with no effective PM observations and are thus removed) have obtained significantly
483 positive downscaling gains ($G_{down} > 0.03$). This hints that the 1-km SSM product can
484 better capture the dynamic behaviors of local ground soil moisture data than the original
485 36-km PM NN-SM data, revealing higher spatial representativeness of the downscaled
486 SSM data product over the country. According to Fig. 4-(b), the mean ubRMSD of all
487 stations is about 0.054 vol/vol, while 90% of those stations have the number lower than
488 0.088 vol/vol. In addition, we made another analysis concerning the possible influence
489 of land cover types on SSM downscaling performance in Fig. 4-(c). The spatial
490 information of land cover types was derived from the MODIS MCD12Q1
491 ([10.5067/MODIS/MCD12Q1.006](https://doi.org/10.5067/MODIS/MCD12Q1.006)) IGBP-based land use image in 2019. For stations
492 that experienced land use change throughout the years of the study period, the ubRMSD
493 is only reported for data in the year of 2019. Clearly, better accuracies are observed
494 mainly in grassland, cropland and bare soil surface, whilst relatively poorer
495 performances (with averages of ubRMSD higher than 0.06 vol/vol) are seen in urban
496 regions, (woody) savanna, and crop-to-natural-vegetation mosaic areas. Such a relative

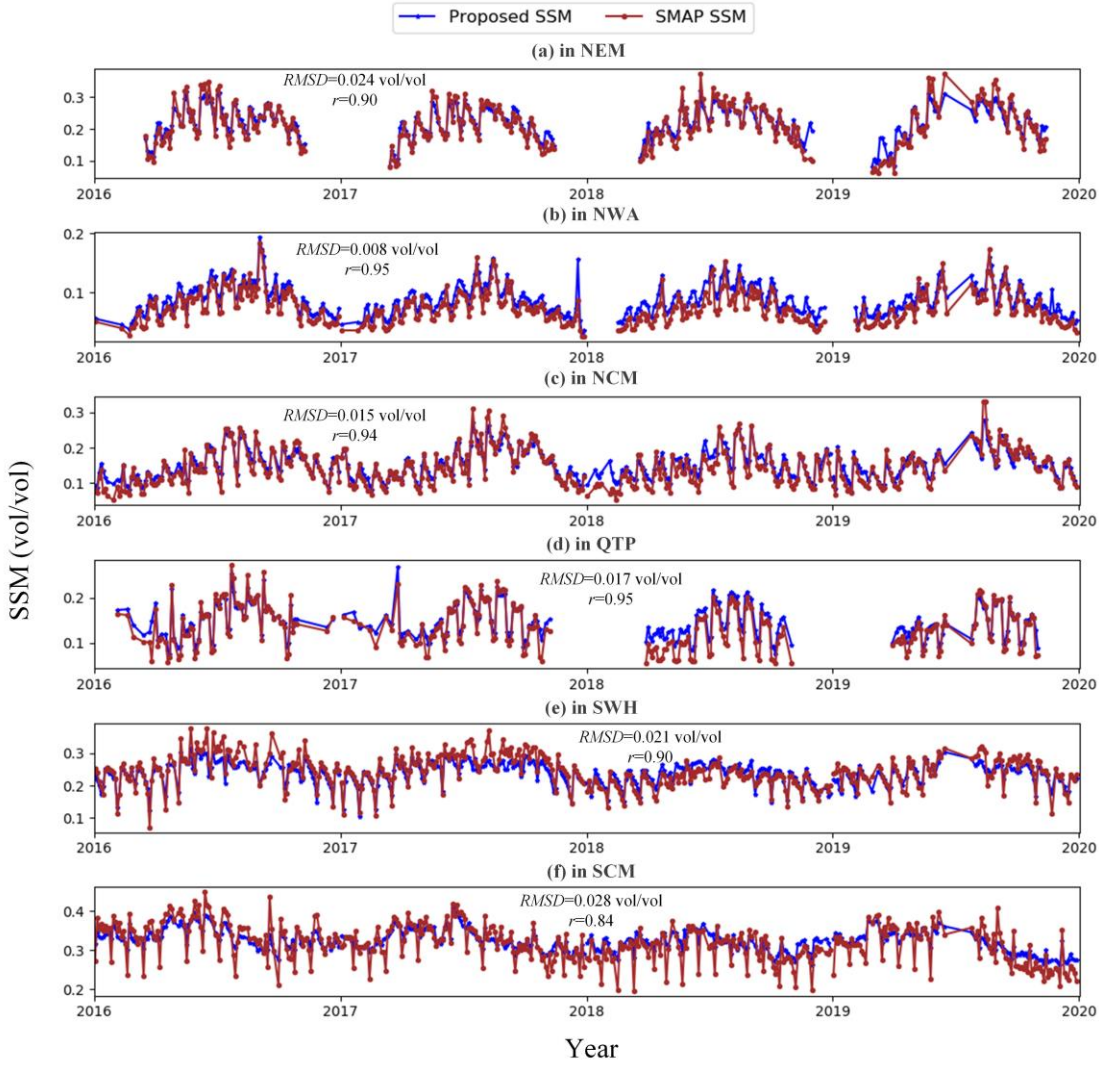
497 performance across land covers is logical because all the land cover types with their
498 average ubRMSD higher than 0.06 vol/vol are characterized by lower hydrologic
499 homogeneity in terms of their definition, e.g. savanna, which is a mixture of grass and
500 tall trees, and urban areas, which are composed of impervious underlying surface.



502 Fig. 4 General validation results of the currently developed SSM product. (a) G_{down} distribution for
503 different stations over China. (b) ubRMSD distribution for different stations over China. (c) ubRMSD
504 statistics reported for different land covers. The numbers in the parentheses of the x-axis labels
505 represent the amount of meteorological stations corresponding to that specific land cover type.

506 In Fig. 5, we compared time series of regionally aggregated SSM from our
507 developed 1-km SSM product to that from the SMAP 36-km descending SSM, for each
508 of the six different geographic-climate regions (as shown in Fig. 1) from 2016 to 2019.

509 Via this effort, we mainly aim to reveal the consistency degree on reflecting soil
510 moisture temporal dynamics at different geographical settings between the two SSM
511 products. This also provides another view to evaluate the reliability of our developed
512 product. Because the SMAP radiometer has a slightly longer revisit cycle (~2-3 days)
513 than AMSR-2, the time series data are also aggregated and averaged at the temporal
514 dimension, with a displayed revisit cycle equal to three days. Overall, the time series
515 data correlate well with each other for all six regions. The relatively lower RMSDs
516 (<0.02 vol/vol) are found in regions with comparatively sparser vegetation covers
517 including the NWA region, the QTP region, and the NCM region. For other three dense-
518 vegetation regions, the performances of our developed product are slightly poorer. This
519 is especially the case for the SCM region, with a lower r -value of 0.84. The reason can
520 be attributed to the enlarged difference on penetration depth into the soil layers between
521 L-band (SMAP) and C-/X-/K- band (AMSR-2) emissions under dense vegetation
522 covers (Ulaby and Wilson, 1985).



523

524 Fig. 5 Time series of SSM aggregated at each of the 6 different geographic-climate regions (as
 525 shown in Fig.1) in China for our developed 1-km product as well as for the SMAP 36-km SSM dataset.

526 The time series range from 2016 to 2019, with a revisit cycle of three days.

527 In Fig. 6-(b) we employed the downscaled SSM image on May 29, 2018, as an
 528 example to demonstrate the spatial features of the developed product. Meanwhile, we
 529 also show the map of SMAP/Sentinel combined SSM (SPL2SMAP_S_V3) obtained
 530 from May 26 to May 31, 2018 in Fig. 6-(a), as a contemporaneous comparison reference.

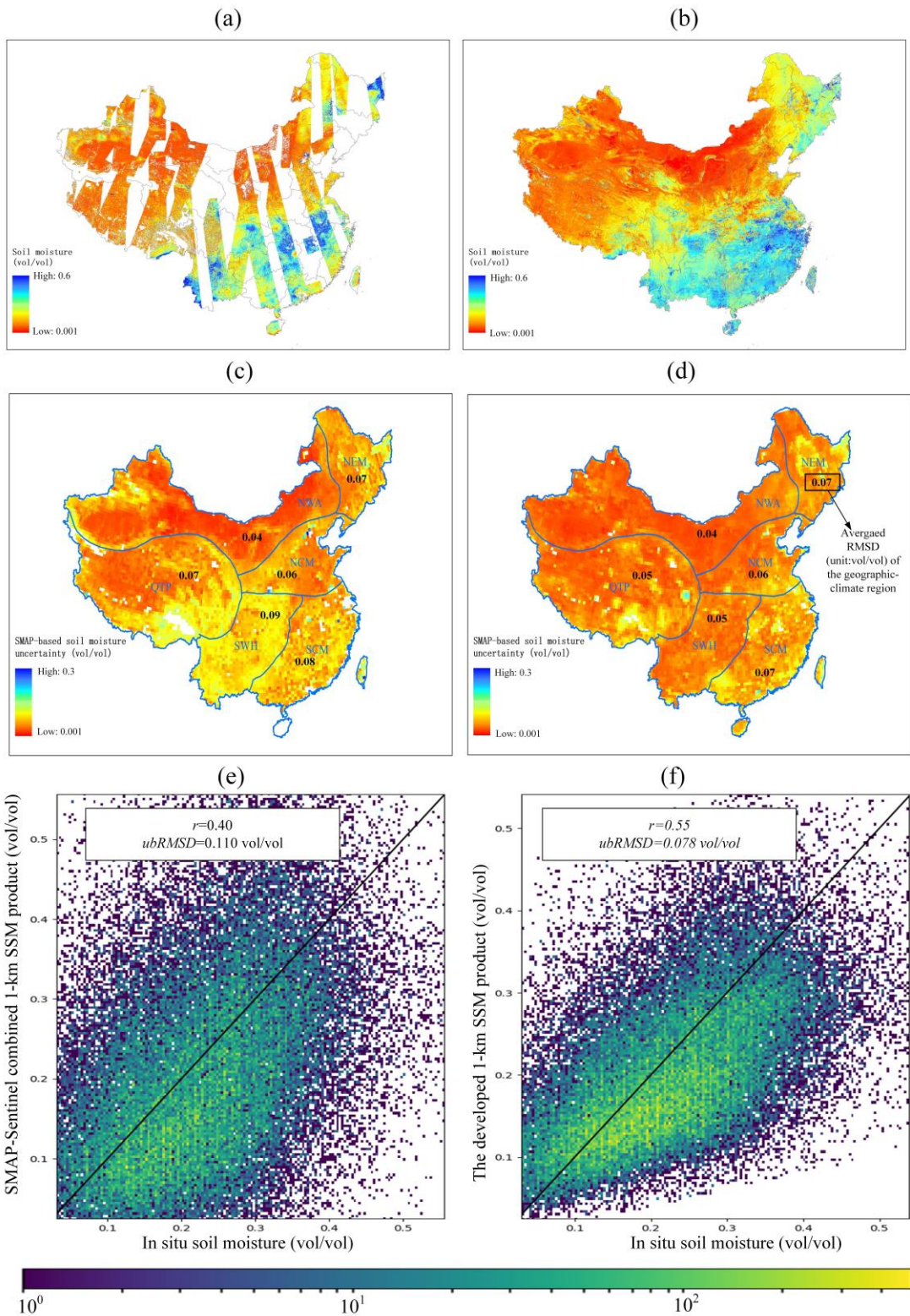
531 Clearly, the SPL2SMAP_S_V3 map has a much lower coverage percentage over the
 532 study region compared with the map of the currently developed product on one single

533 date, even though the former was generated based on multi-date images. Both maps
534 show similar spatial texture depicting the relatively dry climate in northwestern China
535 compared with the humid climate in the Middle-lower Yangtze River Plain.
536 Nevertheless, there also exist cases where the details in texture differ prominently, like
537 that in the far northeastern end of the country.

538 For the sake of further analysis on this point, results of the quantitative comparison
539 as proposed in Section 2.1.3 and Section 2.1.4, is demonstrated in Fig. 6-(c), -(d), -(e),
540 and -(f). Fig. 6-(c) and -(d) show the RMSD maps of the two respective products against
541 SMAP radiometer-based SSM estimates at the 36-km pixel scale. For both products it
542 is manifested that compared with the lower averaged RMSD of 0.04 vol/vol in the
543 NWA region, the uncertainty can increase (shown in yellow) in the densely vegetated
544 NEM and the SCM regions, with averaged RMSDs of 0.07-0.08 vol/vol. However, our
545 developed product has noticeably lower RMSD (0.05 vol/vol) than the
546 SPL2SMAP_S_V3 data (0.07-0.09 vol/vol) in the SWH and part of the QTP regions.
547 Considering their relatively higher elevations, it may be roughly drawn that our
548 downscaled SSM product is more reliable than that downscaled based on active-passive
549 microwave combined datasets in areas with increased topographic effects. Fig. 6-(e)
550 shows that the currently developed SSM product obtained a 0.078 vol/vol ubRMSD
551 and a correlation coefficient of 0.55 against the in-situ soil moisture measurements. It
552 converges more apparently to the 1:1 line when compared with validation result of the
553 SPL2SMAP_S_V3 dataset in Fig. 6-(f). As with the area of China, therefore, the

554 currently developed product is generally superior to the global SMAP/Sentinel

555 combined SSM in terms of both coverage percentage and estimate accuracy.



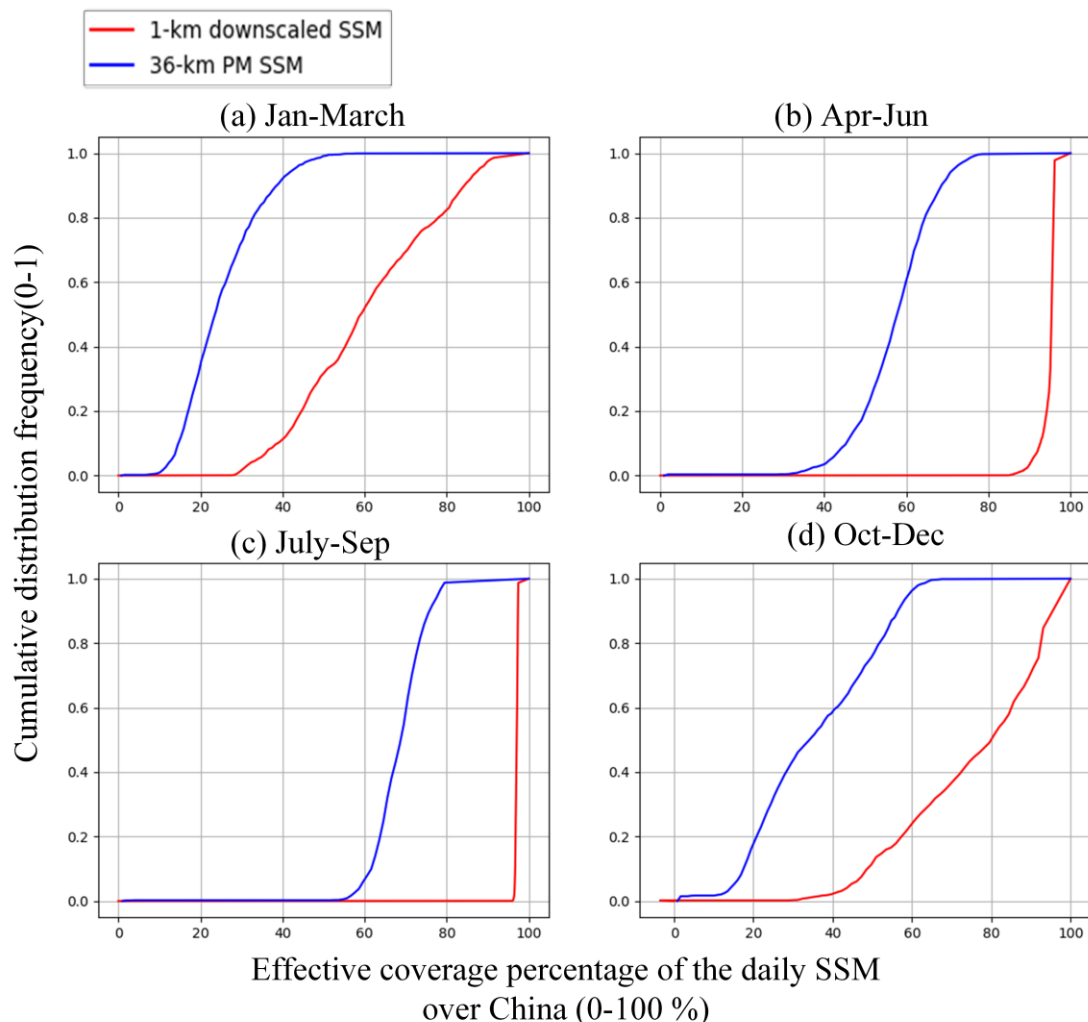
556

557 Fig. 6 Comparison results between the currently developed 1-km SSM product and the SMAP/Sentinel
 558 combined 1-km SSM (SPL2SMAP_S_V3). (a) SPL2SMAP_S_V3 SSM images over China at about
 559 6:00 a.m. synthesized by 6 continuous dates from May 26, 2018 to May 31, 2018. (b) The SSM image at

560 1:30 a.m. of May 29, 2018 from the currently developed product. (c) Spatial uncertainty (RMSD) map
561 of the SPL2SMAP_S_V3 product against SMAP radiometer-based SSM retrievals at the 36-km pixel
562 scale over China for years of 2017, 2018, and 2019. (d) Same to (c) but for validation of the currently
563 developed SSM product. The black numbers in each of the geographic-climate regions indicate
564 averaged uncertainty (RMSD, unit: vol/vol) of the region. (e) Validation results of the
565 SPL2SMAP_S_V3 product against in-situ soil moisture measurements over China for years of 2017,
566 2018, and 2019. The black solid line is the 1:1 line. (f) Same to (e) but for validation of the currently
567 developed SSM product.

568 In Fig. 7, we display the cumulative distribution frequency of coverage
569 percentages of the downscaled SSM product and of the original PM NN-SM product
570 for each season. We should be noted that in this statistical scheme, pixels identified as
571 static water body by the MODIS MCD12Q1 land cover type product were not
572 considered in the denominator of the coverage percentage. Besides, the gap time
573 between the respective on-orbit period of AMSR-E and of AMSR-2 (from October
574 2011 to June 2012, during which there are no effective observations from the PM NN-
575 SM product) were also excluded. It is apparent that in Fig. 7-(b) and -(c), almost all
576 downscaled daily SSM images over the 16-17 years have achieved a coverage
577 percentage higher than 85%. In comparison, the majority of the PM NN-SM daily
578 images have their coverage percentages below 80% over the study region, primarily
579 due to the PM-seam gaps particularly existing in low latitudes (see Section 2.2.2). In
580 Fig. 7-(a) and -(d), the percentages of effective pixels in both the PM and the
581 downscaled SSM images are far lower than their counterparts in the other two

582 subfigures. This is mainly ascribed to extreme meteorological conditions including
 583 snow, ice, and frozen soils that are typically persistent throughout most of these
 584 specified months in the northwestern regions of China. Such conditions can impede
 585 reliable estimates of SSM based on all satellite remote sensing techniques in the current
 586 time. The above inter-seasonal differences on data coverage are also reflected in Fig. 8
 587 in another manner based on presenting the spatial distributions of number percentages
 588 of available dates in each three-month period.



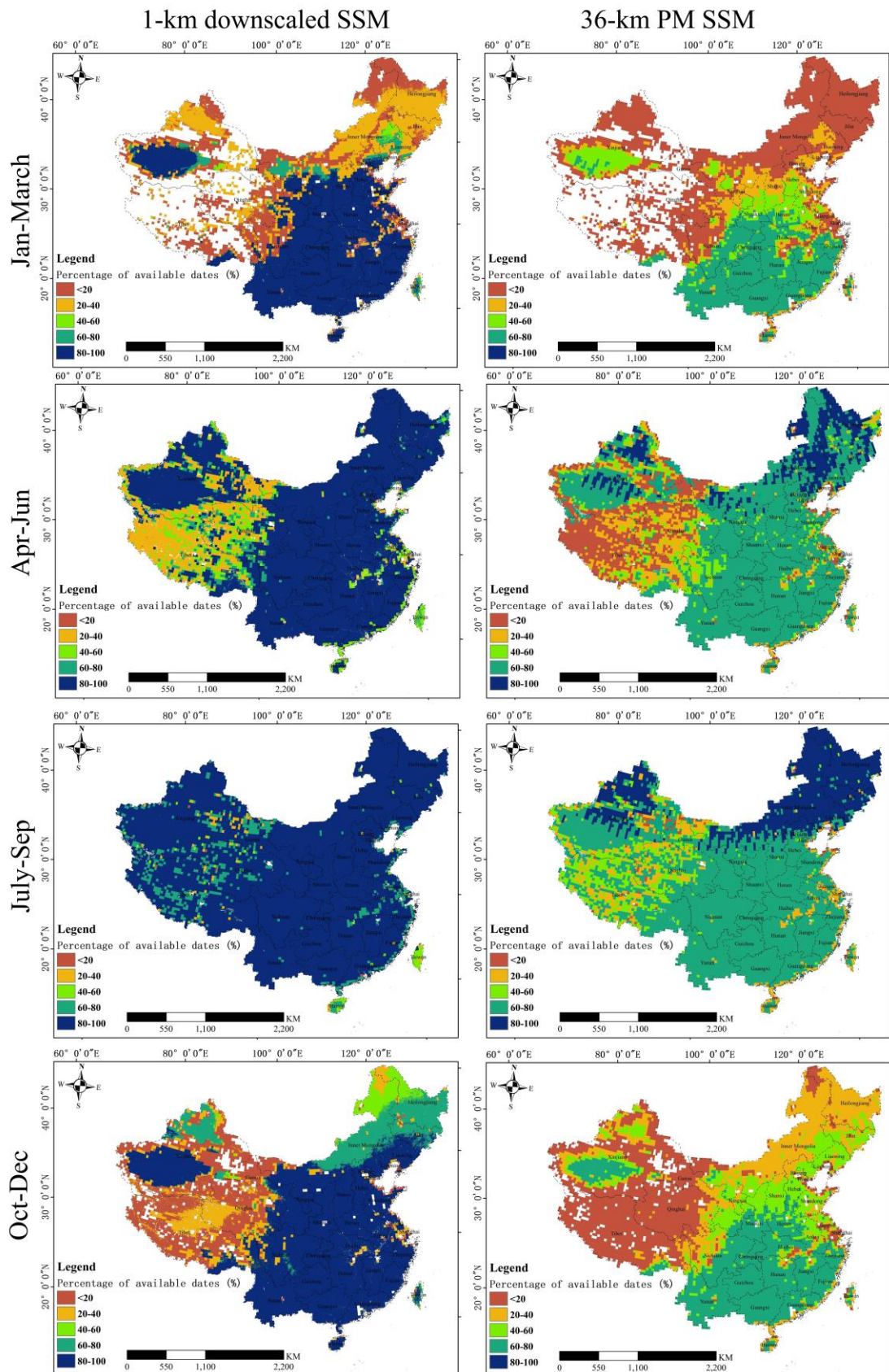
589

590 Fig. 7 Cumulative distribution frequency of our proposed SSM product against the original 36-km SSM

591 product for different seasons. The period between October 2011 and June 2012 is excluded in the

592 current statistics.

593



597 periods (i.e., January-March, April-June, July-September, October-December) of a year are treated

598 respectively. The period between October 2011 and June 2012 is excluded.

599 The techniques behind coverage improvement of the downscaled SSM (against

600 PM and optical data inputs) can be categorized into two classes, i.e. cloud gap-filling

601 of the input optical datasets (see Section 2.2.1), as well as the filling of downscaled

602 SSM in PM-seam gaps (see Section 2.2.2). Table 2 reports the specific validation results

603 (using averages of ground measurements at all stations) of downscaled SSM in these

604 coverage-improved conditions, relative to that generated without using any coverage

605 improvement technique, in order to evaluate the propagated effect of such techniques

606 on the final product. The very limited difference for ubRMSD values (0.053 vol/vol

607 versus 0.056 vol/vol) between cloudy and clear-sky conditions suggest that the 1-km

608 SSM estimates from our final product are generally compatible between cloudy and

609 clear-sky conditions. The downscaled SSM estimated for regions of PM-seam gaps

610 have a slightly worse (but still acceptable) accuracy, considering its ubRMSD of 0.059

611 vol/vol compared to the 0.052 vol/vol ubRMSD of the PM-observed 1-km pixels. In

612 summary of Fig. 7 and Table 2, the currently developed product has achieved a

613 substantially improved spatial coverage against the original remote sensing input

614 datasets, whilst successfully preserved the SSM downscaling accuracy of the

615 observation-covered pixels at the same time.

616 Table 2 Comparisons between validation results for pixels under coverage-improved regions and
617 for pixels under remote-sensing-observation-covered regions.

Evaluation metric*	Comparison between cloudy and clear-sky conditions		Comparison between passive microwave (PM) observed regions and regions of PM-seam gaps	
	Clear-sky condition	Cloudy condition	PM-observed regions	PM-seam gaps
ubRMSD (vol/vol)	0.053	0.056	0.052	0.059
Correlation coefficient	0.49	0.47	0.49	0.44

618 *All evaluation metrics in this column indicate the average of all available stations

619 **4. Discussion**

620 **4.1 Uncertainty on SSM evaluation between satellite- and 621 ground- scales**

622 In this study, we made evaluations on remote sensing SSM products at different
623 spatial resolutions, using measurements from 2000+ stations provided by the national-
624 level soil moisture observation network of China as standard benchmark. Through the
625 evaluations, a ubRMSD of 0.074 vol/vol is reported for the original 36-km NN-SM
626 SSM product (Fig.A1-b). We notice that this result is considerably poorer if compared
627 with another previous evaluation campaign targeting at the same product (Yao et al.,
628 2021), which achieved a global RMSE (RMSD) of 0.029 vol/vol. However, this
629 difference is not unexpected because the two campaigns were carried out in different
630 regions of the world. Also, that particular study (Yao et al., 2021) was conducted based
631 on completely different ground soil moisture observations provided by the International

632 Soil Moisture Network (ISMN) (Dorigo et al., 2021). Compared to the observation
633 network employed in this study, the observation sites of ISMN are more intensively
634 distributed as an “integrated soil moisture station” so as to provide spatially average
635 soil moisture within a grid of tens of kilometers. In this regard, we admit that the ISMN
636 is generally more professional in evaluating satellite PM-based SSM retrievals at a
637 coarser resolution. But on the other hand, only a few (≤ 4) of such “integrated stations”
638 have been set up sporadically within China, making the ISMN data much less
639 representative of our study region compared with the national-level soil moisture
640 network of China exploited by our current study.

641 Although the higher RMSD of the national-level soil moisture network of China
642 may indicate larger measurement uncertainty than the ISMN, the negative influence
643 that might be imposed on our study purpose should be inconsequential. This is because
644 we focus more on the relative validation performance of different SSM products, rather
645 than on the absolute value of any evaluation metric including ubRMSD and correlation
646 coefficient calculated against ground measurements. Specifically, the 1-km downscaled
647 SSM obtained an average ubRMSD of about 0.054 vol/vol among different stations
648 according to Fig. 4-(b). Besides, result of the evaluation in Fig. 6-(d) based on
649 combination of multi-station ground measurements shows a global ubRMSD of 0.078
650 vol/vol for this product. Overall, the above-mentioned results can be identified as at
651 least comparable to the global (multi-station based) ubRMSD of 0.074 vol/vol of the
652 original NN-SM data as they are evaluated against the same benchmark. Therefore,
653 conclusion is safely drawn that the currently developed product preserves the retrieval

654 accuracy of the coarse-resolution NN-SM data, whilst improving the spatial
655 representativeness of the latter product substantially according to the mostly positive
656 G_{down} values in Fig. 4-(a).

657 Moreover, one may also argue that the r -value of 0.55 for the currently developed
658 product in Fig. 6-(d) is not sufficiently high compared with several previous studies
659 (Wei et al., 2019; Sabaghy et al., 2020) obtaining r -values above 0.7 for temporal
660 analysis of satellite remote sensing soil moisture. However, we should be noticed that
661 these previous studies have conducted analyses respectively at the temporal and the
662 spatial dimensions. Based on their results, the spatial analysis typically derived lower
663 r -values (<0.4) compared to that at the temporal dimension. This is probably because
664 the heterogeneity degree of remote sensing pixels can vary significantly across different
665 sites. Since the evaluation in Fig. 5-(d) was deployed at the ‘spatio-temporal’ integrated
666 dimensions, such an r -value is expected. This is also close to the global r -value of 0.6
667 for validation of the coarse-resolution NN-SM product as reported in Yao et al. (2021).

668 **4.2 Uncertainty on cloud gap-filling and validations of LST**

669 As mentioned in Section 2.2.1, LST gap-filled based on the STDF method was
670 used alone as one of the main input datasets for SSM downscaling under cloudy weather.
671 Although such LST inputs contain clear-sky bias from the real cloudy condition, it
672 performs better in driving the SSM downscaling model compared with its bias-adjusted
673 counterpart (see Section Appendix-B for details). The reason may be linked to one of
674 the basic theories behind our SSM downscaling methodology, i.e. the “universal
675 triangle feature space (UTFS)” theory (Carlson et al., 1994). In the UTFS, clear-sky

676 LST is employed to implicitly quantify the surface soil wetness degree as it correlates
677 with the dynamics of soil evaporative efficiency and soil thermal inertia when
678 vegetation cover density is fixed. Under cloudy conditions, however, the satellite
679 observed LST is subjected to not only surface soil property, but also to that related to
680 cloud insulation effect from solar incoming radiation and ground long wave outgoing
681 radiation. As a result, the actual relationship between SSM and cloudy LST could be
682 much more complicated than the one that has been described by the UTFS-based SSM
683 downscaling model (i.e. Equation-2). In comparison, LST generated by the STDF alone
684 for assumed clear-sky conditions, as is free from interference of cloud, would be a
685 comparatively more competent input variable for driving the UTFS-based SSM
686 downscaling model under non-rainy clouds. This is especially the case for thin and
687 short-time clouds with marginal direct feedbacks on surface soil wetness.

688 However, we admit that the STDF-filled LST under rainy clouds is also not suitable
689 for our study purpose. This may explain the slightly higher RMSD for SSM under cloud
690 based on STDF-filled LST (0.056 vol/vol) compared to that under real clear sky (0.053
691 vol/vol), as shown in Table 2. In reality, the actual negative influence of cloud on the
692 final SSM product may be even more serious than indication from the above RMSD
693 difference (i.e. $0.056 - 0.053 = 0.003$ vol/vol), due to the portion of “clear/cloudy-
694 weather-mixed” spatial windows during the fitting process of the downscaling model.
695 In these windows, uncertainty in cloud gap-filled LST may affect accuracy of the fitted
696 model coefficients and thus deteriorate the final SSM estimates in clear-sky pixels
697 within the same window. Consequently, the above RMSD difference has been more or

698 less underestimated. Despite all of above, in our study area of China we regard the
699 STDF-filled LST as a more optimal proxy of heat flux for estimating SSM under clouds,
700 compared to the bias-adjusted LST. On the other hand, future efforts are encouraged to
701 further clarify the mechanical relationships between STDF-filled/bias-adjusted LST
702 and soil wetness degree under clouds.

703 Different from a number of previous studies (Jiménez et al., 2017; Dowling et al.,
704 2021; Yang et al., 2019) validating satellite thermal-infrared-based LST based on
705 longwave radiation observations made at footprint-level observation stations (e.g. flux
706 towers), our study has used 0-cm top ground temperatures as the primary benchmark
707 for this validation campaign instead. Similar to that for SSM validation, the most crucial
708 motivation driving such an experimental design is the significantly intensive
709 distribution of the meteorological stations compared to the very limited number of
710 active and effective flux towers available in China. It is noted that these measurement
711 devices at all of the meteorological stations are required to have been instrumented
712 under open environmental conditions with relatively lower fraction of tall trees and
713 water bodies, in order to conduct efficient monitoring at the physics of near-surface air.
714 This can also be reflected in Fig.4-(c), which reveals no stations built within forest
715 covers. Moreover, as we only focus on the mid-night scenario when the states of all
716 land observations are “most stable” during one diurnal cycle, uncertainties due to the
717 possible temperature inconsistency between bare ground surface and high tree surface
718 as well as due to the temporal mismatch (from about 1:30 to 2:00 A.M.) should have

719 marginal effect on our results. We have carried an extra test that can confirm this
720 discussion, with the detailed procedures described in Section Appendix-C.

721 **4.3 Major novelty, unique profit, and future prospect of the**
722 **developed product**

723 Compared with the widely known active/passive microwave combined SSM
724 product (e.g. the SPL2SMAP_S_V3) and other PM/optical-data combined counterparts
725 which were also published recently but at the monthly scale (Meng et al., 2021), the
726 major novelty of the currently developed product mainly lies in the fact that it has
727 achieved progress on all of the three crucial dimensions of satellite remote sensing,
728 including the temporal revisit cycle (daily), the spatial resolution (1-km), and the quasi-
729 complete coverage under all-weather conditions. To our knowledge, this has rarely been
730 achieved by previously developed satellite soil moisture product at regional scales. For
731 realization of the above-mentioned progresses, we have fused the SSM downscaling
732 framework with other techniques including cloud gap-filling of thermal infrared LST,
733 MWS-based temporal filtering of vegetation indices, as well as reconstruction of seams
734 between neighboring PM swaths in low latitudes. The final SSM estimates under cloudy
735 conditions and intersected with the PM-seam gaps were specially validated against the
736 rest estimates under clear sky and in the regions covered by PM observations,
737 respectively (Table 2). The comparable performances among all treatment groups
738 herein confirm that the accuracy of the product is stable and consistent among all
739 weather conditions.

740 With improvement achieved at the three dimensions, unique profit of the currently
741 developed product can be taken by subsequent studies and various industrial
742 applications. For example, the capability of this product can be investigated on
743 capturing the short-term anomaly of local hydrological signals as well as improved
744 monitoring on drought disasters, which used to be investigated mainly at a coarser
745 resolution by PM SSM (Scaini et al., 2015; Champagne et al., 2011; Albergel et al.,
746 2012). For another, taking advantage of its all-weather daily time series, the product
747 can be utilized together with precipitation data to isolate and quantify the anthropic
748 influence on regional water resources from the natural hydrological dynamics.
749 Examples of such anthropic signals include agricultural irrigation activities, as well as
750 finer-scale information on agricultural crops which was previously interpreted based on
751 PM-driven techniques (Song et al., 2018). In addition, we should realize the important
752 role of soil moisture as a constraint for accurate estimation of surface
753 evapotranspiration and runoff (Zhang et al., 2020; Zhang et al., 2019). Therefore, the
754 profit of this product can be further enhanced if coupled with land-atmosphere coupled
755 models to produce new insights into water-cycle processes of earth surface at a finer
756 spatio-temporal scale.

757 There are still some limitations on our current product to be further improved. First,
758 there may exist the ‘mosaic effect’ at the original PM (36-km) pixel edge. As mentioned
759 in Section 2.2.2, we have used a parameter of ‘spatial square window (ws)’ in Equation-
760 (3) to minimize this negative effect. However, it is still difficult to utterly avoid such
761 negative effect. This is a challenge for all existing SSM downscaling methods (Molero

762 et al., 2016; Stefan et al., 2020; Peng et al., 2016), especially considering the large
763 spatial scale of our study and all uncertainties discussed in Sections 4.1 and 4.2. Besides,
764 other negative influences can be imposed by potential imperfections identified from the
765 original PM product, e.g. from PM SSM retrievals in the QTP region with complicated
766 topography, melt snow or partially frozen soils that cannot be completely screened
767 out by the original product flag in winter. For these extreme conditions, the accuracy
768 of the downscaled SSM may need further validation campaigns like field surveys and
769 experiments, based on which the data quality flag can be better built for the product's
770 future version.

771 The methodological framework proposed in this paper is prospective to be
772 universally applied in other regions of the world to serve for better monitoring of the
773 global surface wetness in the following studies. If applied in continental and global
774 scales, however, the current process for gap-filling of PM seams may require further
775 attention and improvement. In this study, SSM in regions intersected with PM-seam
776 gaps were estimated using TB observations from PM swaths at neighboring dates (see
777 Equation-5). Although the errors in the PM-seam gaps over China as reported by Table
778 2 are only slightly larger compared to the PM-covered regions, they cannot be ignorable
779 completely and may leave extra concern on the universality of this technique, especially
780 in the low latitudinal tropical regions where the effect of PM-seam gap is more apparent
781 than in our study area. Besides, another imperfection of this data product lies in the gap
782 period between AMSR-E and AMSR-2. Considering the different systematic error
783 patterns of various PM SSM products, we did not generate downscaled SSM based on

784 other PM products (e.g. the SMOS SSM product) during this period but just left the
785 period as null values. We suggest a more rigorous and universal inter-calibration
786 framework on different PM SSM products to be developed in the future for a long-term
787 consistent 1-km downscaled SSM dataset.

788 **5. Conclusions**

789 This paper describes the main technical procedures of a recently developed remote
790 sensing surface soil moisture (SSM) product over China covering the recent ten years
791 and more. Based on combination of passive microwave SSM downscaling theory and
792 other related remote sensing techniques, the product achieves multi-dimensional
793 distinctive features including 1-km resolution, daily revisit cycle, and quasi-complete
794 all-weather coverage. These were rarely satisfied completely by other existing remote
795 sensing SSM product at regional scales. Validations were conducted against
796 measurements from 2000+ automatic soil moisture observation stations over China.
797 Overall, an average ubRMSD of 0.054 vol/vol across different stations is reported for
798 the currently developed product. The mostly positive G_{down} values show this product
799 has significantly improved spatial representativeness against the 36-km PM SSM data
800 (a major source for downscaling). Meanwhile, it generally preserves the retrieval
801 accuracy of the 36-km data product. Moreover, additional validation results show that
802 the currently developed product surpasses the widely used SMAP-sentinel combined
803 global 1-km SSM product, with a correlation coefficient of 0.55 achieved against that
804 of 0.40 for the latter product. At the regional scale, time series patterns of our developed

805 data product are highly correlated with that of the widely recognized SMAP radiometer-
806 based SSM for all geographic settings. The methodological framework for product
807 generation is promising to be applied at the continental and global scales in the future,
808 and the product is potential to benefit various research/industrial fields related to
809 hydrological processes and water resource management.

810

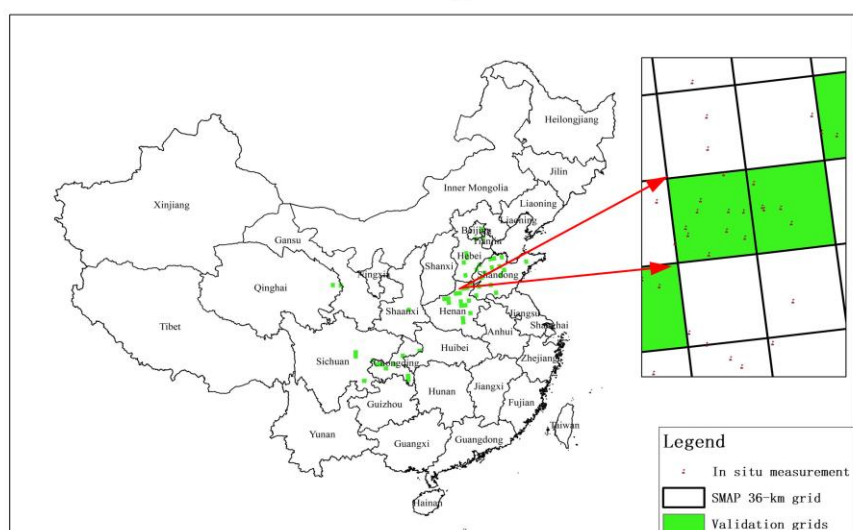
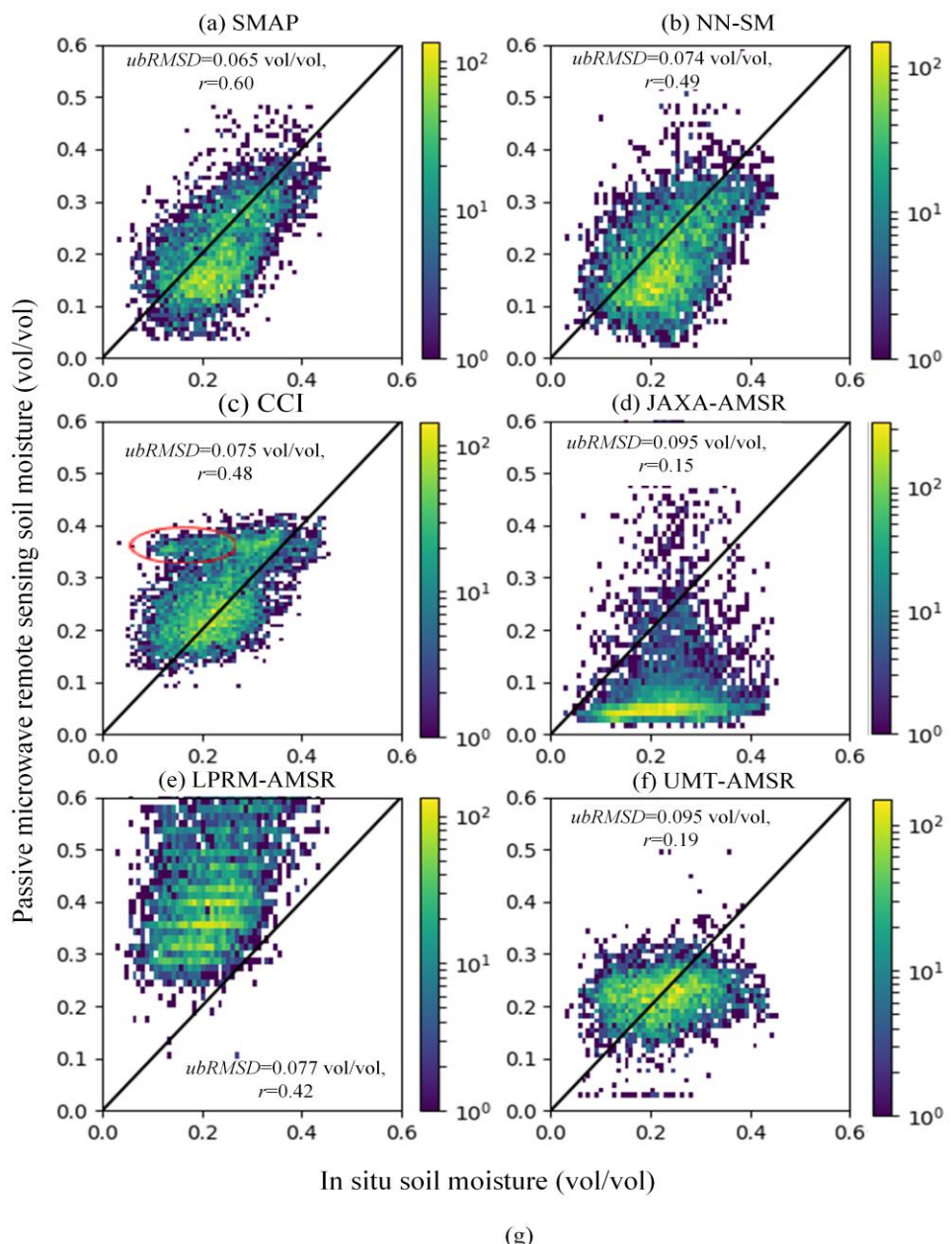
811 **Appendix**

812 **A. Evaluation on different PM SSM products**

813 We have made evaluations on the various AMSR-based SSM products (as shown
814 in Table 1) covering the recent 10 years or longer, based on our soil moisture
815 observation network all over China. The SMAP radiometer-based SSM dataset, as
816 described in Section 2.1.4, was also evaluated as a reference. The evaluation period
817 covers the three years of 2017, 2018, and 2019. All AMSR-based 25-km grids were re-
818 set to the SMAP 36-km grid system using the nearest resampling method. Only grids
819 that contain equal or more than 4 soil moisture measurement stations were employed,
820 in which, the grid-based PM SSM estimate was compared with average of
821 measurements from all interior stations. Finally, 53 grids were selected, as shown by
822 the green color in Fig.A1-(g). For AMSR-based products, only the mid-night
823 descending datasets were evaluated, whilst for the SMAP product, our evaluation only
824 focused on its descending mode in the early morning.

825 As manifested by Fig.A1-(a) to -(f), the selected SSM product in the current study,
826 i.e., the NN-SM product has an unbiased RMSD of 0.074 vol/vol and a correlation
827 coefficient of 0.49. This obviously outperforms the other three traditional AMSR-based
828 SSM products (i.e. JAXA-AMSR, LPRM-AMSR, and UMT-AMSR products) and is
829 only inferior to the SMAP SSM retrievals, whilst the later only covers the latest period
830 since 2015. As far as CCI data are concerned, it has a similar performance against the
831 selected NN-SM in general. Nevertheless, the region marked by red circle in Fig.A1-

832 (c) indicates that CCI estimates have a considerably larger proportion of overestimated
833 anomalies. But overall, the primary reason that we have abandoned CCI but selected
834 NN-SM is because the latter can provide a higher coverage fraction of valid pixels in
835 our study region, as has been stated in Section 2.1.1.



837 Fig. A1 (a)-(f) Comparison of different PM SSM products (as reported in Table 1) against the in situ
838 SSM measurements in China. (g) Locations of the 36-km EASE-GRID-projection based pixels used for
839 this comparison campaign.

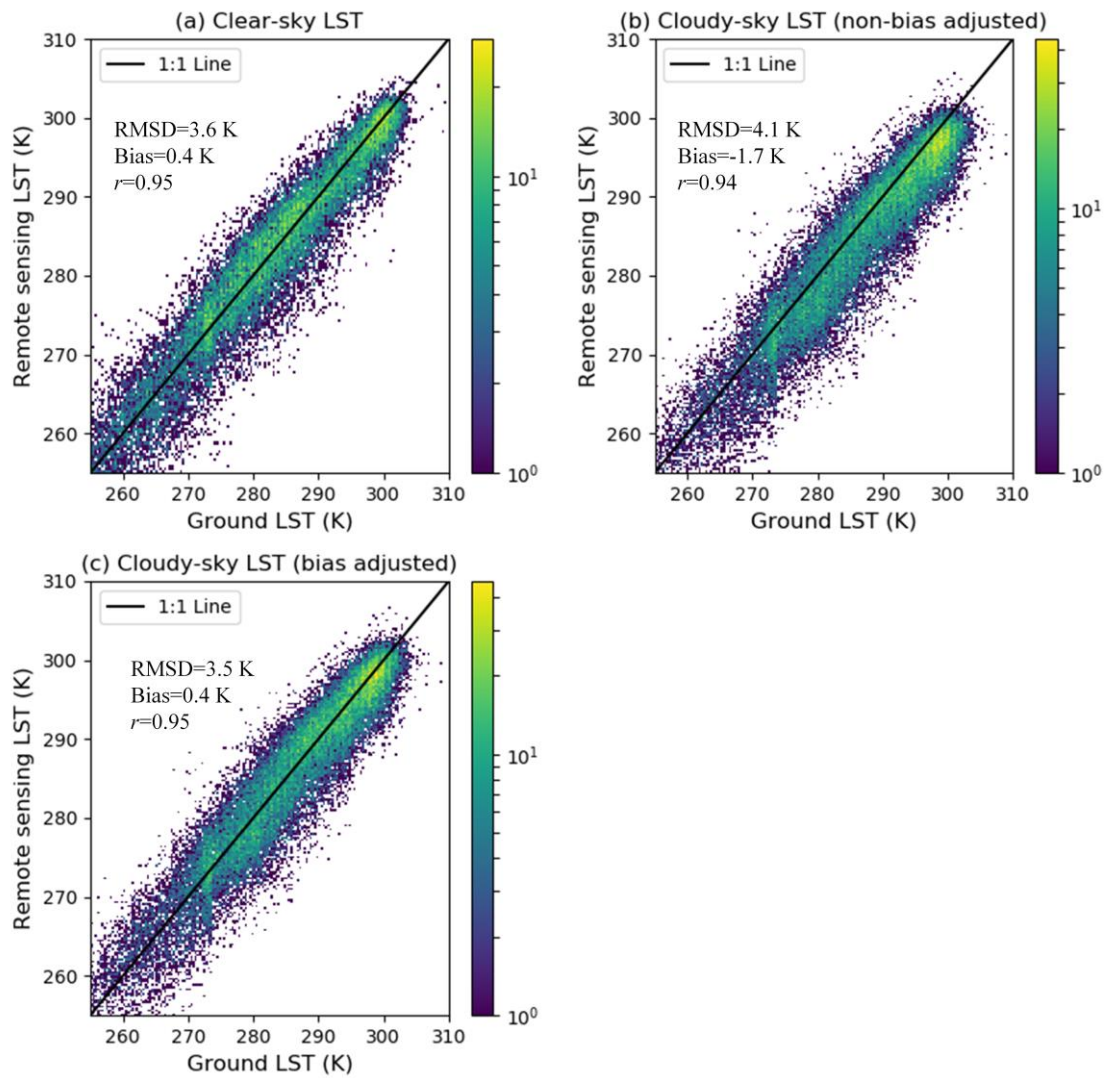
840 **B. Evaluation on the influence of bias adjustment for**
841 **reconstructed ‘clear-sky’ LST under cloud**

842 In Section 2.2.2, we have emphasized that the gap-filled LST for cloudy pixels
843 reflects the theoretical surface temperature of that pixel under a hypothetical clear-sky
844 condition. As this cloud gap-filled LST would suffer from a possible bias against the
845 real surface temperature under cloud (Dowling et al., 2021), we made an additional
846 experiment regarding to further improvement of this cloud gap-filled LST. The follow-
847 up step for bias adjustment of this hypothetical clear-sky LST (but actually under
848 cloudy conditions), as expounded in Section 4.2 of Dowling et al. (2021), was
849 conducted herein using remote sensing and in situ LST data over China but only in
850 2018. We illustrate the validation results for bias adjusted and non-bias adjusted LST
851 under cloudy conditions in Fig. A2-(b) and -(c), respectively. Similar to Fig. 3,
852 validation results for clear-sky LST of that year are also displayed (Fig. A2-(a)) for
853 comparison. The results generally show that the follow-up step is effective in reducing
854 the bias of the originally gap-filled ‘clear-sky LST’ under cloudy conditions (from -1.7
855 K to 0.4 K).

856 In the subsequent step, we substituted the original non-bias adjusted LST under
857 cloudy conditions with its bias adjusted counterpart, and used the latter as the input for
858 SSM downscaling. The general validation results of the downscaled SSM are illustrated

859 in Fig. A3 (similar to that presented in Fig. 4-a and -b). Contrary to the above-analyzed
860 Fig. A2, the bias adjusted cloudy LST with better gap-filling accuracies, however,
861 obtained inferior performance in SSM downscaling. This final validation result, to
862 some degree, confirms our assumption in Section 2.2.2 that the reconstructed cloudy
863 LST but for the hypothesized clear-sky condition is the better proxy of surface moisture
864 dynamics. But overall, as all LST estimates discussed herein are for the midnight
865 scenario (when the energy interaction between atmosphere and land surface is relatively
866 weak), the RMSD difference for different weather conditions in Fig.A2 is expectedly
867 marginal. As a consequence, the difference in ubRMSD of SSM in Fig.A3 can hardly
868 be identified as ‘very significant’. Therefore, we encourage further tests on this
869 conclusion in specific future studies to confirm its universality, especially for situation
870 of the ‘morning to noon’ time window.

871



872

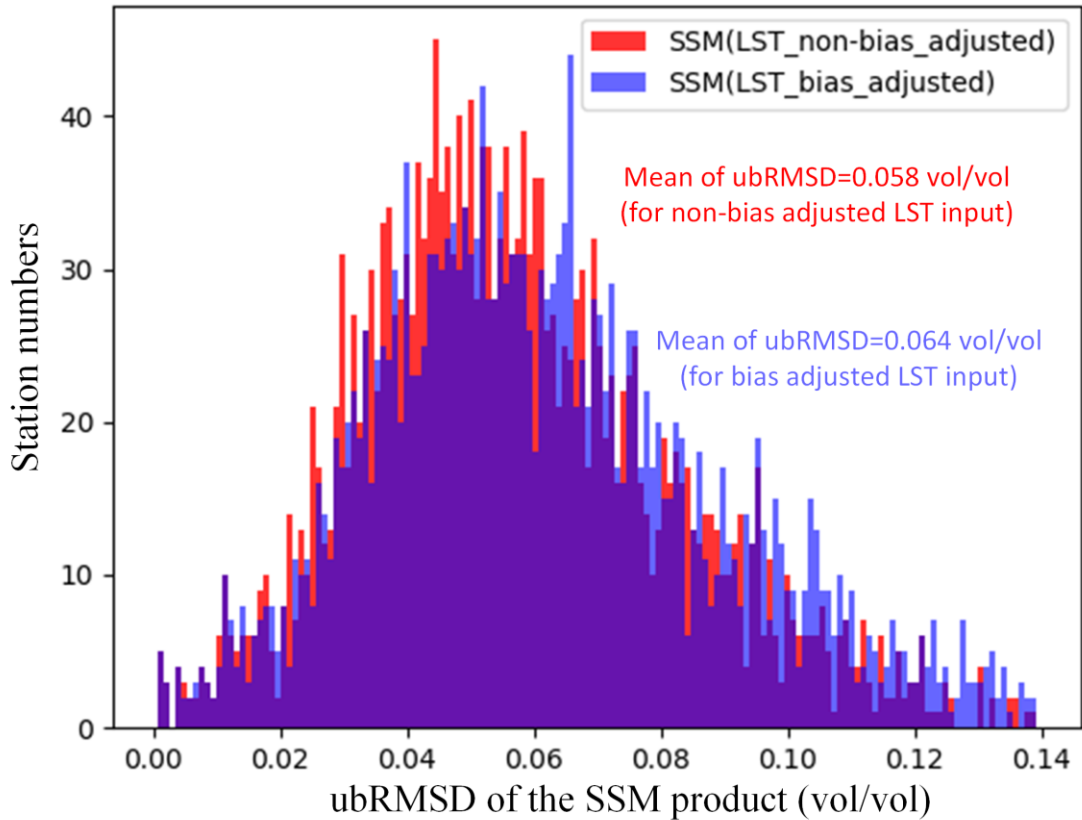
873 Fig. A2 Validation of the clear sky LST (a), reconstructed LST under cloud but with no passive-

874 microwave based bias adjustment (b), as well as the reconstructed LST under cloud with passive-

875 microwave based bias adjustment (c) respectively, based on the 0-cm ground temperature

876 measurements at meteorological stations.

877



878

879 Fig. A3 The statistical distribution of ubRMSD at different stations for SSM estimates driven by two
 880 respective kinds of cloudy LST inputs.

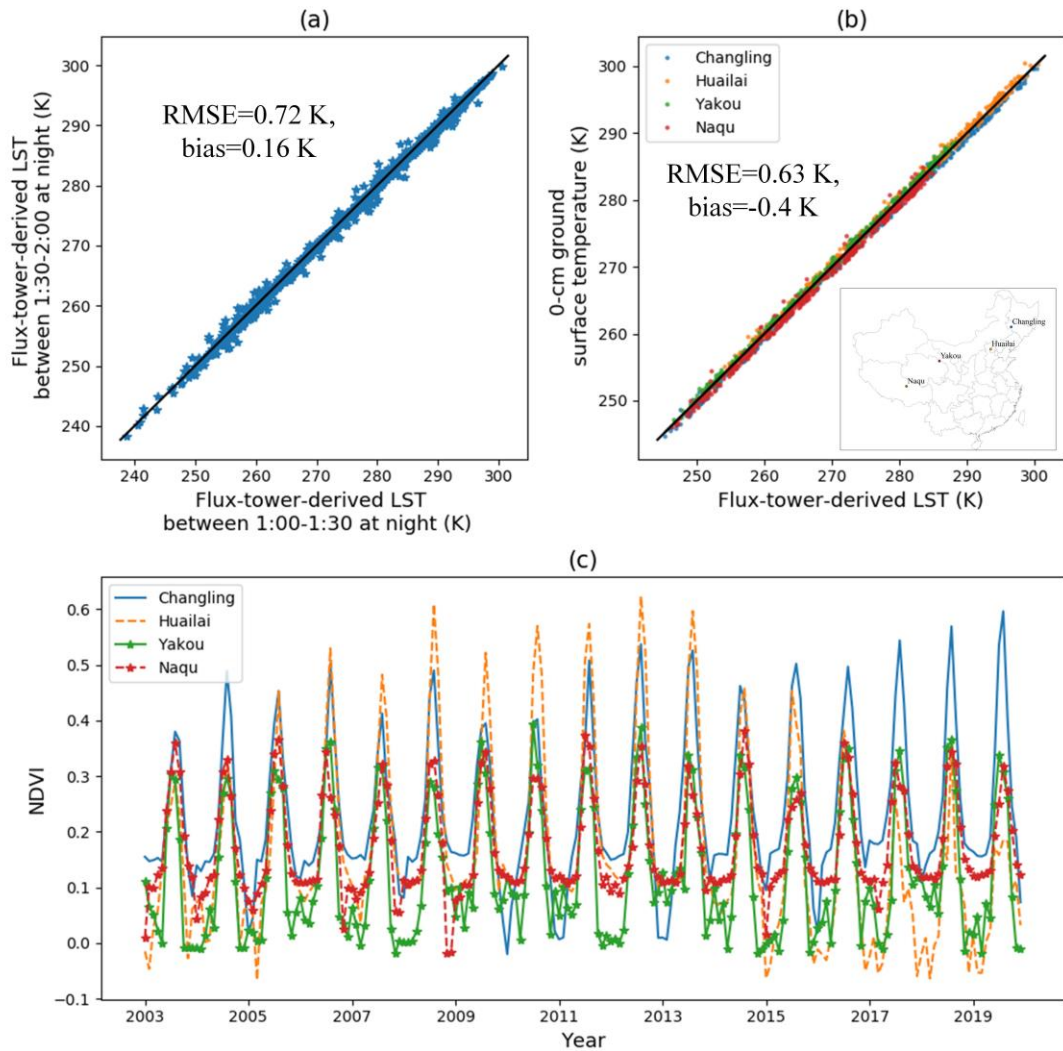
881 **C. Uncertainty test between 0-cm ground temperature
 882 observations and flux-tower-derived thermal infrared LST**

883 We herein utilized 4 flux towers to calculate their footprint-level (about 500-1000
 884 m) thermal infrared LST based on long wave radiation measurements, plus broad band
 885 emissivity data derived from the MODIS MYD21A1 product (MYD21A1N.V061).

886 The 4 towers are all characterized by moderate or low vegetation (grassland) and are
 887 dispersedly located at different eco-regions of China, namely the towers of Changling,
 888 Huailai, Yakou, and Naqu (see the inset map in Fig.A4-b). Data from Changling are
 889 derived from the FLUXNET community ([FLUXNET2015 Dataset - FLUXNET](#)) in 2010.

890 Data from the other three towers are derived from the National Tibetan Plateau Data
891 Center, with data DOIs of <http://dx.doi.org/10.11888/Meteoro.tpdc.271094> for Huailai
892 in 2018, <http://dx.doi.org/10.11888/Meteoro.tpdc.270781> for Yakou in 2018, and
893 <http://dx.doi.org/10.11888/Meteoro.tpdc.270910> for Naqu in 2016. These data have
894 been preprocessed by their providers to record the dynamics of those variables at a half-
895 hour interval. The algorithm for calculating LST based on flux-tower-derived long
896 wave radiation is inherited from Wang and Liang (2009). We first compared the flux-
897 tower-derived night-time LST estimates between 1:00-1:30 A.M. and 1:30-2:00 A.M..
898 As shown by Fig.A4-(a), the very slight RMSD of 0.72 K suggests that LST is generally
899 stable between 1:00 and 2:00 A.M. at night. In Fig.A4-(b), we also found marginal bias
900 and RMSD within 1 K between average flux-tower-derived LST of 1:00- 2:00 A.M.
901 and the corresponding 0-cm ground temperature at close meteorological sites (within 1
902 km and at 2:00 A.M.).

903 In Fig.A4-(c) we demonstrate time series for monthly average NDVI (derived as
904 in Section 2.2.1) at the 1-km pixels containing each of the four sites from 2003-2019.
905 Clearly, there are very rare cases with NDVI values exceeding 0.5, corroborating the
906 “open environmental conditions” met by the meteorological stations. In view of above,
907 it is feasible for our study to have used the 0-cm ground temperature at pixels of such
908 moderate to low vegetation covers as the evaluation benchmark of the satellite-derived
909 thermal infrared LST.



910

911 Fig. A4 (a) Comparison of LST between 1:00-1:30 A.M. and 1:30-2:00 A.M. for the four selected flux
 912 towers. (b) Comparison of flux-tower-derived LST averaged for 1:00-2:00 A.M. at the four towers and
 913 corresponding night-time 0-cm ground temperature at proximal meteorological stations. The inset map
 914 shows the location of the four flux towers. (3) Monthly NDVI time series for 1-km pixels containing
 915 each of the four flux towers.

916

917 Author contributions

918 Peilin Song and Yongqiang Zhang designed the research and developed the whole
 919 methodological framework; Peilin Song and Yongqiang Zhang supervised the
 920 processing line of the 1-km SSM product; Jianping Guo and Bingtong provided in situ

921 soil moisture data for validation; Peilin Song wrote the original draft of the manuscript;
922 Yongqiang Zhang, Peilin Song, Jiancheng Shi, and Tianjie Zhao revised the manuscript.

923 **Competing interests**

924 The authors declare that they have no conflict of interest.
925

926 **Data availability**

927 The published SSM dataset is available under the Creative Commons Attribution
928 4.0 International License at the following link:
929 <http://dx.doi.org/10.11888/Hydro.tpdc.271762> (Song and Zhang, 2021b). This dataset
930 covers all of China's terrestrial area at a daily revisit frequency (about 1:30 A.M. at
931 local time) and a 1km spatial resolution from January 2003 to October 2011 and from
932 July 2012 to December 2019.

933 **Acknowledgement**

934 The authors would like to thank the National Aeronautics and Space
935 Administration (NASA) for providing all MODIS and DEM data sets free of charge.

936 **Financial support**

937 This study was jointly supported by the National Natural Science Foundation of
938 China (Grant No. 42001304), the Open Fund of State Key Laboratory of Remote
939 Sensing Science (Grant No. OFSLRSS202117), CAS Pioneer Talents Program, CAS-

940 CSIRO International Cooperation Program, and the International Partnership Program
941 of Chinese Academy of Sciences (Grant No. 183311KYSB20200015).
942

943 **References**

944 Albergel, C., de Rosnay, P., Gruhier, C., Munoz-Sabater, J., Hasenauer, S., Isaksen, L., . . . Wagner, W.: Evaluation
945 of remotely sensed and modelled soil moisture products using global ground-based in situ observations, *Remote Sens.*
946 *Environ.*, 118, 215-226, 10.1016/j.rse.2011.11.017, 2012.

947 Brunsdon, C., Fotheringham, A. S., and Charlton, M. E.: Geographically weighted regression: A method for exploring
948 spatial nonstationarity, *Geogr. Anal.*, 28, 281-298, 1996.

949 Busch, F. A., Niemann, J. D., and Coleman, M.: Evaluation of an empirical orthogonal function-based method to
950 downscale soil moisture patterns based on topographical attributes, *Hydrological Processes*, 26, 2696-2709, 2012.

951 Carlson, T. N., Gillies, R. R., and Perry, E. M.: A method to make use of thermal infrared temperature and NDVI
952 measurements to infer surface soil water content and fractional vegetation cover, *Remote sensing reviews*, 9, 161-173, 1994.

953 Champagne, C., McNairn, H., and Berg, A. A.: Monitoring agricultural soil moisture extremes in Canada using passive
954 microwave remote sensing, *Remote Sens. Environ.*, 115, 2434-2444, 2011.

955 Chauhan, N. S., Miller, S., and Ardanuy, P.: Spaceborne soil moisture estimation at high resolution: a microwave-
956 optical/IR synergistic approach, *Int. J. Remote Sens.*, 24, 4599-4622, <http://doi.org/10.1080/0143116031000156837>, 2003.

957 Chen, Y., Yuan, H., Yang, Y., and Sun, R.: Sub-daily soil moisture estimate using dynamic Bayesian model averaging,
958 *J. Hydrol.*, 590, 125445, <https://doi.org/10.1016/j.jhydrol.2020.125445>, 2020.

959 Choi, M. and Hur, Y.: A microwave-optical/infrared disaggregation for improving spatial representation of soil
960 moisture using AMSR-E and MODIS products, *Remote Sens. Environ.*, 124, 259-269,
961 <http://doi.org/10.1016/j.rse.2012.05.009>, 2012.

962 Das, N., Entekhabi, D., Dunbar, R. S., Kim, S., Yueh, S., Colliander, A., . . . Cosh, M.: SMAP/Sentinel-1 L2
963 Radiometer/Radar 30-Second Scene 3 km EASE-Grid Soil Moisture, Version 3 [dataset],
964 <https://doi.org/10.5067/ASB0EQQ2LYJV>, 2020.

965 Das, N. N., Entekhabi, D., Dunbar, R. S., Chaubell, M. J., Colliander, A., Yueh, S., . . . Thibeault, M.: The SMAP and
966 Copernicus Sentinel 1A/B microwave active-passive high resolution surface soil moisture product, *Remote Sens. Environ.*,
967 233, 111380, <https://doi.org/10.1016/j.rse.2019.111380>, 2019.

968 den Besten, N., Steele-Dunne, S., de Jeu, R., and van der Zaag, P.: Towards Monitoring Waterlogging with Remote
969 Sensing for Sustainable Irrigated Agriculture, *Remote Sens.*, 13, 2021.

970 Dorigo, W., Himmelbauer, I., Aberer, D., Schremmer, L., Petrakovic, I., Zappa, L., . . . Sabia, R.: The International
971 Soil Moisture Network: serving Earth system science for over a decade, *Hydrol. Earth Syst. Sci.*, 25, 5749-5804,
972 10.5194/hess-25-5749-2021, 2021.

973 Dowling, T. P. F., Song, P., Jong, M. C. D., Merbold, L., Wooster, M. J., Huang, J., and Zhang, Y.: An Improved Cloud
974 Gap-Filling Method for Longwave Infrared Land Surface Temperatures through Introducing Passive Microwave
975 Techniques, *Remote Sens.*, 13, 3522, 2021.

976 Du, J. Y., Kimball, J. S., and Jones, L. A.: Passive microwave remote sensing of soil moisture based on dynamic
977 vegetation scattering properties for AMSR-E, *IEEE Trans. Geosci. Remote Sens.*, 54, 597-608, 2016.

978 Duan, S. and Li, Z.: Spatial Downscaling of MODIS Land Surface Temperatures Using Geographically Weighted
979 Regression: Case Study in Northern China, *IEEE Trans. Geosci. Remote Sens.*, 54, 6458-6469,
980 <http://doi.org/10.1109/TGRS.2016.2585198>, 2016.

981 Entekhabi, D., Reichle, R. H., Koster, R. D., and Crow, W. T.: Performance Metrics for Soil Moisture Retrievals and
982 Application Requirements, *J. Hydrometeorol.*, 11, 832-840, 10.1175/2010jhm1223.1, 2010a.

983 Entekhabi, D., Das, N., Kim, S., Jagdhuber, T., Piles, M., Yueh, S., . . . Martínez-Fernández, J.: High-Resolution
984 Enhanced Product based on SMAP Active-Passive Approach and Sentinel 1A Radar Data, *AGU Fall Meeting Abstracts*,
985 H24C-08,

986 Entekhabi, D., Njoku, E. G., O'Neill, P. E., Kellogg, K. H., Crow, W. T., Edelstein, W. N., . . . Van Zyl, J.: The Soil
987 Moisture Active Passive (SMAP) Mission, *Proc. IEEE*, 98, 704-716, <http://doi.org/10.1109/JPROC.2010.2043918>, 2010b.

988 Fang, B. and Lakshmi, V.: Passive Microwave Soil Moisture Downscaling Using Vegetation and Surface Temperatures,
989 *Vadose Zone J.*, 12, 1712-1717, 2013.

990 Fang, B., Lakshmi, V., Bindlish, R., and Jackson, T.: AMSR2 Soil Moisture Downscaling Using Temperature and
991 Vegetation Data, *Remote Sens.*, 10, 2018.

992 Fang, B., Lakshmi, V., Bindlish, R., Jackson, T. J., Cosh, M., and Basara, J.: Passive Microwave Soil Moisture
993 Downscaling Using Vegetation Index and Skin Surface Temperature, 2013.

994 Fujii, H., Koike, T., and Imaoka, K.: Improvement of the AMSR-E Algorithm for Soil Moisture Estimation by
995 Introducing a Fractional Vegetation Coverage Dataset Derived from MODIS Data, *Journal of the Remote Sensing Society*
996 of Japan

997 Im, J., Park, S., Rhee, J., Baik, J., and Choi, M.: Downscaling of AMSR-E soil moisture with MODIS products using
998 machine learning approaches, *Environ Earth Sci*, 75, 1-19, <http://doi.org/10.1007/s12665-016-5917-6>, 2016.

999 Ines, A. V. M., Das, N. N., Hansen, J. W., and Njoku, E. G.: Assimilation of remotely sensed soil moisture and vegetation
1000 with a crop simulation model for maize yield prediction, *Remote Sens. Environ.*, 138, 149-164, 10.1016/j.rse.2013.07.018,
1001 2013.

1002 Jeffrey, P., Walker, Paul, R., and Houser: A methodology for initializing soil moisture in a global climate model:
1003 Assimilation of near-surface soil moisture observations, *Journal of Geophysical Research Atmospheres*, 2001.

1004 Jiménez, C., Prigent, C., Ermida, S. L., and Moncet, J. L.: Inversion of AMSR-E observations for land surface
1005 temperature estimation: 1. Methodology and evaluation with station temperature, *Journal of Geophysical Research:
1006 Atmospheres*, 2017.

1007 Jing, Z. and Zhang, X.: A soil moisture assimilation scheme using satellite-retrieved skin temperature in meso-scale
1008 weather forecast model, *Atmos Res*, 95, 333-352, 2010.

1009 Jones, L. A., Kimball, J. S., Podest, E., McDonald, K. C., Chan, S. K., and Njoku, E. G.: A method for deriving land
1010 surface moisture, vegetation optical depth, and open water fraction from AMSR-E, *IEEE IGARSS 2009.*, Cape Town,
1011 South Africa, 2009, III-916-III-919, <http://doi.org/10.1109/IGARSS.2009.5417921>,

1012 Jung, M., Reichstein, M., Ciais, P., Seneviratne, S. I., Sheffield, J., Goulden, M. L., . . . Zhang, K.: Recent decline in
1013 the global land evapotranspiration trend due to limited moisture supply, *Nature*, 467, 951-954, 10.1038/nature09396, 2010.

1014 Kim, J. and Hogue, T. S.: Improving spatial soil moisture representation through integration of AMSR-E and MODIS
1015 products, *IEEE Trans. Geosci. Remote Sens*, 50, 446-460, <http://doi.org/10.1109/TGRS.2011.2161318>, 2012.

1016 Koike, T., Nakamura, Y., Kaihatsu, I., Davva, G., Matsuura, N., Tamagawa, K., and Fujii, H.: Development of an
1017 Advanced Microwave Scanning Radiometer (AMSR-E) algorithm of soil moisture and vegetation water content (written
1018 in Japanese), *Annual Journal of Hydraulic Engineering*, 48, 217-222 2004.

1019 Komatsu, T. S.: Toward a Robust Phenomenological Expression of Evaporation Efficiency for Unsaturated Soil
1020 Surfaces, *Journal of Applied Meteorology*, 42, 1330-1334, 10.1175/1520-0450(2003)042<1330:Tarpeo>2.0.Co;2, 2003.

1021 Kong, D., Zhang, Y., Gu, X., and Wang, D.: A robust method for reconstructing global MODIS EVI time series on the
1022 Google Earth Engine, *Isprs J Photogramm*, 155, 13-24, 2019.

1023 Koster, R. D., Mahanama, S., Livneh, B., Lettenmaier, D. P., and Reichle, R. H.: Skill in streamflow forecasts derived
1024 from large-scale estimates of soil moisture and snow, *Nature Geoscience*, 3, 613-616, 2010.

1025 Malb  teau, Y., Merlin, O., Molero, B., R  diger, C., and Bacon, S.: DisPATCh as a tool to evaluate coarse-scale remotely
1026 sensed soil moisture using localized in situ measurements: Application to SMOS and AMSR-E data in Southeastern
1027 Australia, *Int J Appl Earth Obs*, 45, 221-234, <https://doi.org/10.1016/j.jag.2015.10.002>, 2016.

1028 Meesters, A. G. C. A., De Jeu, R. A. M., and Owe, M.: Analytical derivation of the vegetation optical depth from the
1029 microwave polarization difference index, *IEEE Geosci. Remote Sens. Lett.*, 2, 121-123, 2005.

1030 Mendoza, P. A., Mizukami, N., Ikeda, K., Clark, M. P., Gutmann, E. D., Arnold, J. R., . . . Rajagopalan, B.: Effects of
1031 different regional climate model resolution and forcing scales on projected hydrologic changes, *J. Hydrol.*, 541, 1003-1019,
1032 <https://doi.org/10.1016/j.jhydrol.2016.08.010>, 2016.

1033 Meng, X. J., Mao, K. B. A., Meng, F., Shi, J. C., Zeng, J. Y., Shen, X. Y., . . . Guo, Z. H.: A fine-resolution soil moisture
1034 dataset for China in 2002-2018, *Earth System Science Data*, 13, 3239-3261, 10.5194/essd-13-3239-2021, 2021.

1035 Merlin, O., Al Bitar, A., Walker, J. P., and Kerr, Y.: An improved algorithm for disaggregating microwave-derived
1036 soil moisture based on red, near-infrared and thermal-infrared data, *Remote Sens. Environ.*, 114, 2305-2316,
1037 <https://doi.org/10.1016/j.rse.2010.05.007>, 2010.

1038 Merlin, O., Walker, J. P., Chehbouni, A., and Kerr, Y.: Towards deterministic downscaling of SMOS soil moisture
1039 using MODIS derived soil evaporative efficiency, *Remote Sens. Environ.*, 112, 3935-3946,
1040 <http://doi.org/10.1016/j.se.2008.06.012>, 2008.

1041 Merlin, O., Chehbouni, A. G., Kerr, Y. H., Njoku, E. G., and Entekhabi, D.: A combined modeling and
1042 multipectral/multiresolution remote sensing approach for disaggregation of surface soil moisture: Application to SMOS
1043 configuration, *IEEE Trans. Geosci. Remote Sens.*, 43, 2036-2050, <http://doi.org/10.1109/TGRS.2005.853192>, 2005.

1044 Merlin, O., Escorihuela, M. J., Mayoral, M. A., Hagolle, O., Al Bitar, A., and Kerr, Y.: Self-calibrated evaporation-
1045 based disaggregation of SMOS soil moisture: An evaluation study at 3 km and 100 m resolution in Catalunya, Spain,
1046 *Remote Sens. Environ.*, 130, 25-38, 10.1016/j.rse.2012.11.008, 2013.

1047 Merlin, O., Malb  teau, Y., Notfi, Y., Bacon, S., Er-Raki, S., Khabba, S., and Jarlan, L.: Performance Metrics for Soil
1048 Moisture Downscaling Methods: Application to DISPATCH Data in Central Morocco, *Remote Sens.*, 7, 3783-3807,
1049 <http://doi.org/10.3390/rs70403783>, 2015.

1050 Molero, B., Merlin, O., Malb  teau, Y., Al Bitar, A., Cabot, F., Stefan, V., . . . Jackson, T. J.: SMOS disaggregated soil
1051 moisture product at 1km resolution: Processor overview and first validation results, *Remote Sens. Environ.*, 180, 361-376,
1052 <http://doi.org/10.1016/j.rse.2016.02.045>, 2016.

1053 Montaldo, N., Albertson, J. D., Mancini, M., and Kiely, G.: Robust simulation of root zone soil moisture with
1054 assimilation of surface soil moisture data, *Water Resour Res.*, 37, 2889-2900, 10.1029/2000WR000209, 2001.

1055 O'Neill, P. E., Bindlish, R., Chan, S., Chaubell, J., Colliander, A., Njoku, E., and Jackson, T.: SMAP Algorithm

1056 Theoretical Basis Document: Level 2 & 3 Soil Moisture (Passive) Data Products, Revision G., Jet Propulsion Laboratory,

1057 Pasadena, CA, 2021.

1058 Owe, M., de Jeu, R., and Walker, J.: A methodology for surface soil moisture and vegetation optical depth retrieval

1059 using the microwave polarization difference index, *IEEE Trans. Geosci. Remote Sens.*, 39, 1643-1654, 2001.

1060 Pan, H., Chen, Z., Wit, A. D., and Ren, J.: Joint Assimilation of Leaf Area Index and Soil Moisture from Sentinel-1

1061 and Sentinel-2 Data into the WOFOST Model for Winter Wheat Yield Estimation, *Sensors (Basel, Switzerland)*, 19, 2019.

1062 Peng, J., Loew, A., Zhang, S. Q., Wang, J., and Niesel, J.: Spatial downscaling of satellite soil moisture data using a

1063 vegetation temperature condition index, *IEEE Trans. Geosci. Remote Sens.*, 54, 558-566,

1064 <http://doi.org/10.1109/TGRS.2015.2462074>, 2016.

1065 Piles, M., Entekhabi, D., and Camps, A.: A Change Detection Algorithm for Retrieving High-Resolution Soil Moisture

1066 From SMAP Radar and Radiometer Observations, *IEEE Trans. Geosci. Remote Sens.*, 47, 4125-4131,

1067 10.1109/TGRS.2009.2022088, 2009.

1068 Sabaghy, S., Walker, J. P., Renzullo, L. J., Akbar, R., Chan, S., Chaubell, J., . . . Yueh, S.: Comprehensive analysis of

1069 alternative downscaled soil moisture products, *Remote Sens. Environ.*, 239, 111586,

1070 <https://doi.org/10.1016/j.rse.2019.111586>, 2020.

1071 Sanchez-Ruiz, S., Piles, M., Sanchez, N., Martinez-Fernandez, J., Vall-Ilossera, M., and Camps, A.: Combining SMOS

1072 with visible and near/shortwave/thermal infrared satellite data for high resolution soil moisture estimates, *J. Hydrol.*, 516,

1073 273-283, 10.1016/j.jhydrol.2013.12.047, 2014.

1074 Scaini, A., Sanchez, N., Vicente-Serrano, S. M., and Martinez-Fernandez, J.: SMOS-derived soil moisture anomalies

1075 and drought indices: a comparative analysis using in situ measurements, *Hydrological Processes*, 29, 373-383,

1076 10.1002/hyp.10150, 2015.

1077 Song, P. and Zhang, Y.: An improved non-linear inter-calibration method on different radiometers for enhancing

1078 coverage of daily LST estimates in low latitudes, *Remote Sens. Environ.*, 264, 112626,

1079 <https://doi.org/10.1016/j.rse.2021.112626>, 2021a.

1080 Song, P. and Zhang, Y.: Daily all weather surface soil moisture data set with 1 km resolution in China (2003-2019),

1081 National Tibetan Plateau Data Center [dataset], 10.11888/Hydro.tpdc.271762, 2021b.

1082 Song, P., Huang, J., and Mansaray, L. R.: An improved surface soil moisture downscaling approach over cloudy areas

1083 based on geographically weighted regression, *Agr Forest Meteorol*, 275, 146-158, 10.1016/j.agrformet.2019.05.022, 2019a.

1084 Song, P., Zhang, Y., and Tian, J.: Improving Surface Soil Moisture Estimates in Humid Regions by an Enhanced
1085 Remote Sensing Technique, *Geophys Res Lett*, 48, e2020GL091459, <https://doi.org/10.1029/2020GL091459>, 2021.

1086 Song, P., Mansaray, L. R., Huang, J., and Huang, W.: Mapping paddy rice agriculture over China using AMSR-E
1087 time series data, *Isprs J Photogramm*, 144, 469-482, 10.1016/j.isprsjprs.2018.08.015, 2018.

1088 Song, P., Huang, J., Mansaray, L. R., Wen, H., Wu, H., Liu, Z., and Wang, X.: An Improved Soil Moisture Retrieval
1089 Algorithm Based on the Land Parameter Retrieval Model for Water-Land Mixed Pixels Using AMSR-E Data, *IEEE Trans.*
1090 *Geosci. Remote Sens.*, 1-15, 10.1109/TGRS.2019.2915346, 2019b.

1091 Stefan, V. G., Merlin, O., Escorihuela, M.-J., Molero, B., and Er-Raki, S.: Temporal Calibration of an Evaporation-
1092 Based Spatial Disaggregation Method of SMOS Soil Moisture Data, *Remote Sens.*, 12, 1671, 2020.

1093 Sui, D. Z.: Tobler's First Law of Geography: A Big Idea for a Small World?, *Annals of the Association of American
1094 Geographers*, 94, 269-277, <https://doi.org/10.1111/j.1467-8306.2004.09402003.x>, 2004.

1095 Ulaby, F. T. and Wilson, E. A.: Microwave Attenuation Properties of Vegetation Canopies, *IEEE Trans. Geosci.
1096 Remote Sens.*, GE-23, 746-753, 10.1109/TGRS.1985.289393, 1985.

1097 Vergopolan, N., Xiong, S. T., Estes, L., Wanders, N., Chaney, N. W., Wood, E. F., . . . Sheffield, J.: Field-scale soil
1098 moisture bridges the spatial-scale gap between drought monitoring and agricultural yields, *Hydrol. Earth Syst. Sci.*, 25,
1099 1827-1847, 2021.

1100 Verstraeten, W. W., Veroustraete, F., van der Sande, C. J., Grootaers, I., and Feyen, J.: Soil moisture retrieval using
1101 thermal inertia, determined with visible and thermal spaceborne data, validated for European forests, *Remote Sens.
1102 Environ.*, 101, 299-314, 2006.

1103 Wang, K. and Liang, S.: Evaluation of ASTER and MODIS land surface temperature and emissivity products using
1104 long-term surface longwave radiation observations at SURFRAD sites, *Remote Sens. Environ.*, 113, 1556-1565,
1105 <https://doi.org/10.1016/j.rse.2009.03.009>, 2009.

1106 Wang, L. and Qu, J. J.: NMDI: A normalized multi-band drought index for monitoring soil and vegetation moisture
1107 with satellite remote sensing, *Geophys Res Lett*, 34, L20405, 10.1029/2007GL031021, 2007.

1108 Wei, Z., Meng, Y., Zhang, W., Peng, J., and Meng, L.: Downscaling SMAP soil moisture estimation with gradient
1109 boosting decision tree regression over the Tibetan Plateau, *Remote Sens. Environ.*, 225, 30-44, 2019.

1110 Wu, D., Liang, H., Cao, T., Yang, D., Zhou, W., and Wu, X.: Construction of operation monitoring system of automatic
1111 soil moisture observation network in China, *Meteorological Science and Technology*, 42, 278-282, 2014

1112 Yang, G., Sun, W. W., Shen, H. F., Meng, X. C., and Li, J. L.: An Integrated Method for Reconstructing Daily MODIS
1113 Land Surface Temperature Data, *IEEE J. Sel. Top. Appl. Earth Observ. Remote Sens.*, 12, 1026-1040, 2019.

1114 Yao, P., Lu, H., Shi, J., Zhao, T., Yang, K., Cosh, M. H., . . . Entekhabi, D.: A long term global daily soil moisture

1115 dataset derived from AMSR-E and AMSR2 (2002–2019), *Scientific Data*, 8, 143, 10.1038/s41597-021-00925-8, 2021.

1116 Zeng, Y., Feng, Z., and Xiang, N.: Assessment of soil moisture using Landsat ETM+ temperature/vegetation index in

1117 semiarid environment, *IEEE International Geoscience & Remote Sensing Symposium*, Piscataway NJ, 2004, 4306-4309

1118 vol.4306, 10.1109/IGARSS.2004.1370089,

1119 Zhang, J., Zhou, Z., Yao, F., Yang, L., and Hao, C.: Validating the Modified Perpendicular Drought Index in the North

1120 China Region Using In Situ Soil Moisture Measurement, *IEEE Geoscience & Remote Sensing Letters*, 12, 542-546, 2014.

1121 Zhang, Y., Kong, D., Gan, R., Chiew, F. H. S., McVicar, T. R., Zhang, Q., and Yang, Y.: Coupled estimation of 500 m

1122 and 8-day resolution global evapotranspiration and gross primary production in 2002-2017, *Remote Sens. Environ.*, 222,

1123 165-182, 2019.

1124 Zhang, Y. Q., Chiew, F. H. S., Liu, C. M., Tang, Q. H., Xia, J., Tian, J., . . . Li, C. C.: Can Remotely Sensed Actual

1125 Evapotranspiration Facilitate Hydrological Prediction in Ungauged Regions Without Runoff Calibration?, *Water Resour*

1126 *Res*, 56, 2020.

1127 Zheng, J. Y., Lu, H. S., Crow, W. T., Zhao, T. J., Merlin, O., Rodriguez-Fernandez, N., . . . Gou, Q. Q.: Soil moisture

1128 downscaling using multiple modes of the DISPATCH algorithm in a semi-humid/humid region, *Int J Appl Earth Obs*, 104,

1129 10.1016/j.jag.2021.102530, 2021.

1130 Zhou, S., Williams, A. P., Lintner, B., Berg, A. M., and Gentine, P.: Soil moisture–atmosphere feedbacks mitigate

1131 declining water availability in drylands, *Nature Climate Change*, 11, 2021.

1132 Zhu, Z. and Shi, C.: Simulation and Evaluation of CLDAS and GLDAS Soil Moisture Data in China (written in

1133 Chinese), *Science Technology and Engineering*, 32, 138-144, 2014.

1134